

**Resonance Behavior of Magnetostrictive Sensor in Longitudinal Vibration mode for  
Biological Agent Detection**

by

Madhumidha Ramasamy

A thesis submitted to the Graduate Faculty of  
Auburn University  
in partial fulfillment of the  
requirements for the Degree of  
Master of Science

Auburn, Alabama  
December 13, 2010

Keywords: Magnetostriction, Longitudinal Vibration mode, Biological Agent Detection,  
Numerical Simulation and Resonance Behavior

Copyright 2010 by Madhumidha Ramasamy

Approved by

Bart C. Prorok, Chair, Associate Professor of Materials Engineering  
Dong-Joo Kim, Associate Professor of Materials Engineering  
Pradeep Lall, Professor of Mechanical Engineering

## Abstract

The growing threat of bio warfare agents and bioterrorism has led to the development of specific field tools that perform rapid analysis and identification of encountered suspect materials. One such technology, recently developed is a micro scale acoustic sensor that uses experimental modal analysis. Ferromagnetic materials with the property to change their physical dimensions in response to changing its magnetization can be built into such sensors and actuators. One such sensor is fashioned from Metglas 2826MB, a Magnetostrictive strip actuated in their longitudinal vibration mode when subjected to external magnetic field. Due to mass addition, these magnetostrictive strips are driven to resonance with a modulated magnetic field resulting in frequency shifts. In Vibration Mechanics the frequency shift for a certain amount of mass will have a tolerance limit based on their distribution and discrete position over the sensor platform. In addition, lateral positioning of same amount of mass does not influence the resonant frequency shift of the sensor. This work concentrates on developing a model correlating theoretical, experimental and numerical simulations to determine the mass of *E. Coli O157:H7* cells attached to the sensor platform

## Acknowledgments

I would like to sincerely thank my mentor, Dr. Bart C. Prorok without whom none of this would have been possible. His continuous support, encouragement and valuable suggestions played a vital role in the achievement of this research. I would like to extend my thanks to my advisory committee members, Dr. Dong-joo Kim and Dr. Pradeep Lall for their participation in my thesis committee. I would like thank Mr. Charles Ellis for his financial support in my final semester which was great timely help. I would also like to thank my Research mates Cai, Shaqib, Dong, Bo, Kevin, Nicole and Brandon for their constant support and encouragement during the course of my work.

I take immense pleasure in thanking my family members for believing in me and standing by me at every step till today. Special thanks to Nida for being my strength and making me feel auburn as home away from home. Finally I would like to thank all my friends for their unwavering support and timely help.

## Table of Contents

Abstract.....	ii
Acknowledgments.....	iii
List of Figures.....	vi
List of Tables.....	ix
Chapter 1 Introduction.....	1
1.1 Motivation for Research.....	1
1.2 Overview.....	5
Chapter 2 Literature Review.....	6
2.1 Available Techniques for Bio Species Detection.....	6
2.1.1 Electro-Chemical Sensors.....	8
2.1.2 Optical Sensors.....	9
2.1.3 Mass Sensors.....	12
2.1.3.1 QCM.....	12
2.1.3.2 SAW.....	13
2.1.3.3 Micro cantilever.....	14
2.2 Magnetostrictive Sensors.....	16
2.2.1 Metglas 2628 MB.....	17
2.3 Detection of <i>Escherichia coli</i> .....	19
Chapter 3 Materials and Methods.....	21

3.1 Magnetostriction .....	21
3.2 Longitudinal Vibration Mode .....	22
3.3 Principle of Operation.....	23
3.4 Design and Numerical Simulation .....	28
3.5 Experimental Method.....	30
3.5.1 Glass Bead Attachment.....	32
3.5.2 Detection Setup.....	33
Chapter 4 Results and Discussion.....	35
4.1 Distribution of Mass .....	35
4.1.1 Uniform Distribution .....	36
4.1.2 Non-uniform Distribution .....	38
4.1.2.1 Maximum Frequency Shift .....	39
4.1.2.2 Minimum Frequency Shift.....	46
4.2 Influence of Discrete Position.....	54
4.2.1 Simulation Result.....	54
4.2.2 Experimental Result.....	55
4.2.3 Theoretical Verification .....	56
4.3 Influence of Physical Dimension .....	59
4.3.1 Length Dependence .....	59
4.3.2 Width Dependence.....	61
Chapter 5 Conclusion.....	62
References .....	63

## List of Figures

Figure 1.1 Comparative toxicity of effective doses of biological agents, toxins, and chemical agents bacteria .....	2
Figure 1.2 Distributions, by industry of application, of the relative number of works appeared in the literature on detection of pathogenic bacteria .....	3
Figure 1.3 Distribution, by micro-organism, of the relative number of works appeared in the literature on detection of pathogenic bacteria .....	4
Figure 2.1 Approximate numbers of articles using different techniques to detect and/or identify pathogenic bacteria .....	6
Figure 2.2 Schematic diagram of typical transduction formats employed in biosensors .....	7
Figure 2.3 Diagram of how an amperometric immunofiltration biosensor works .....	9
Figure 2.4 Schematic diagram of a biosensor utilizing surface plasmon resonance (SPR) transduction.....	10
Figure 2.5 Schematic diagram of a biosensor based on piezoelectric transduction .....	12
Figure 2.6 Schematic diagram of a micro cantilever-based biosensor .....	15
Figure 2.7 Magnetostrictive strips used on valued goods for theft protection .....	17
Figure 3.1 SEM images of the Magnetoelastic strips by simple micro fabrication technique ..	18
Figure 3.2 SEM image of <i>E. coli</i> O157:H7 cells .....	20
Figure 3.3 Schematics of a magnetostrictive sensor's response to the applied magnetic.....	21
Figure 3.4 Transverse vs. longitudinal actuation illustrated with a freestanding magnetostrictive strips .....	23
Figure 3.5 Mechanical force analysis in a unit of sensor .....	24
Figure 3.6 Schematic of sensor structure in beam .....	25
Figure 3.7 Effect of Mass attachment on the wave speed of the sensor platform due to longitudinal vibration .....	27

Figure 3.8 Simulation result of a 250 $\mu\text{m}$ x 50 $\mu\text{m}$ x 4 $\mu\text{m}$ sensor meshed with equilateral triangle facets of element size 7.5 $\mu\text{m}$ .....	28
Figure 3.9 Simulation results for freestanding Metglas beam with the size of 250 $\mu\text{m}$ x 50 $\mu\text{m}$ x 4 $\mu\text{m}$ . Poisson's ratio of 0.33 was employed .....	29
Figure 3.10 Procedural steps involved in the Micro fabrication of Magnetostrictive strips for the sensor platform.....	31
Figure 3.11 SEM images showing glass beads attached to the sensor in various locations.....	32
Figure 3.12 Resonant frequency detection setup containing Actuation/read coil, and magnetic bar .....	33
Figure 4.1 SEM image of the sensor platform with the uniform distribution of <i>E.coli</i> cells attached experimentally .....	35
Figure 4.2 Resonant Frequency Shift due to uniform distribution of <i>E.coli</i> cells .....	37
Figure 4.3 SEM image of a sensor with Non-Uniform distribution of <i>E.coli</i> cells .....	38
Figure 4.4 Schematic diagrams representing the non-uniform distribution for the maximum resonant frequency condition .....	39
Figure 4.5 Plots representing the Maximum Resonant Frequency Shift due to Non-uniform and Uniform distribution of <i>E.coli</i> cells .....	44
Figure 4.6 Plots representing the Maximum Resonant Frequency Shift due to Non-uniform distribution of <i>E.coli</i> cells for Numerical Simulation and theoretically calculated results .....	46
Figure 4.7 Schematic diagrams representing the non-uniform distribution for the minimum resonant frequency condition.....	47
Figure 4.8 Plots representing the Minimum Resonant Frequency Shift due to Non-uniform and Uniform distribution of <i>E.coli</i> cells .....	49
Figure 4.9 Plots representing the Minimum Resonant Frequency Shift due to Non-uniform distribution of <i>E.coli</i> cells for Numerical Simulation and theoretically calculated results .....	51
Figure 4.10 Plots representing the Resonant Frequency Shift of the sensor platform of dimension 250 $\mu\text{m}$ x 50 $\mu\text{m}$ x 4 $\mu\text{m}$ due to distribution of mass ( <i>E.coli</i> cells of size 1.43 $\mu\text{m}$ x 0.73 $\mu\text{m}$ x 0.73 $\mu\text{m}$ .) .....	52
Figure 4.11 Addition of concentrated mass at discrete location x on the sensor platform of length L .....	53
Figure 4.12 Plots of Resonant Frequency shift in KHz for the addition of concentrated mass at discrete locations over the sensor platform .....	57
Figure 4.13 Plots of Resonant Frequency shift due to mass distribution over the sensor platform with varying Length.....	59

Figure 4.14 Plots of Resonant Frequency shift due to mass distribution over the sensor platform with varying Width ..... 60



## List of Tables

Table 4.1 Reseonant Frequency shift due to uniform distribution of <i>E.coli</i> cells over the sensor platform .....	36
Table 4.2 Calculated values of $\eta$ and KL with the corresponding resonant frequency shift values determined using the Equation (4.12) and (3.6) .....	43
Table 4.3 Calculated and Simulated Maximum Resonant Frequency Shift results for Non-Uniform Distribution .....	45
Table 4.4 Calculated values of $\eta$ and KL with the corresponding resonant frequency shift values determined using the Equation (4.14) and (3.6) .....	48
Table 4.5 Calculated and Simulated Minimum Resonant Frequency Shift results for Non-Uniform Distribution .....	50
Table 4.6 Test results of sensor (5 mm x 1 mm x 28 $\mu\text{m}$ ) attached with glass bead at different locations .....	54
Table 4.7 The Resonant Frequency values corresponding to concentrated mass on discrete locations .....	57

# CHAPTER 1

## INTRODUCTION

### 1.1. Motivation For Research

The end of cold war has reduced international tension between the super powers. However, there has been a remarkable increase in the production and availability of chemical and biological weapons throughout the world. The combination of these factors has significantly increased the possibility of an attack on the human race involving the use of such weapons. Biological agents are often considered to be psychologically more threatening of the two, and therefore provide more appeal to the terrorist[1]. Biological agents can be manufactured in facilities that are inexpensive to construct; that resemble pharmaceutical, food, or medical production sites; and that provide no detectable sign that such agents are being produced. One characteristic of biological agents that makes them so attractive to potential users is their remarkably low effective dose; that is, the mass of agent that is required to create the desired effect (incapacitation or death) on the target population. Figure 1.1 shows the approximate mass in milligrams (mg) of an agent needed to achieve the desired result in comparison to toxins and chemical agents. The mass of a paper clip is included in this diagram as a point of reference. We can clearly see the vast differences in effectiveness between biological agents (microbial agents, e.g., bacteria and viruses) and chemical agents[2]. At the extreme, some biological agents are as much as 14 *billion* times more effective than chemical agents, making it easy to see why biological agents are often described as the poor man's atomic bomb. It is also noticed that if a terrorist chooses to use a toxin agent (in order to get relatively rapid effects in a tactical situation), a much greater mass of the toxin agent will have to be employed than if biological

agents were being used. This mass of toxin agent in some cases may be equivalent to chemical agent masses.

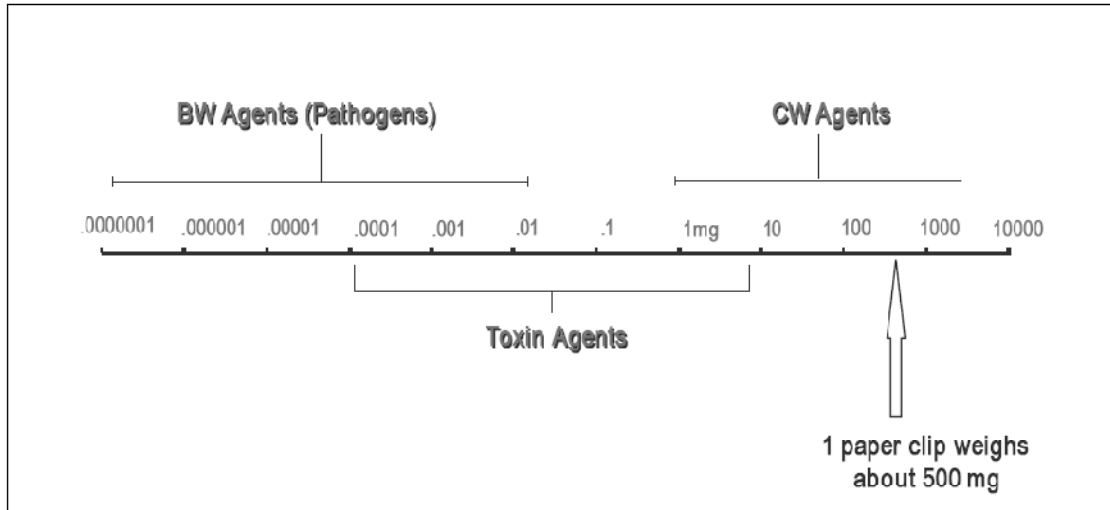
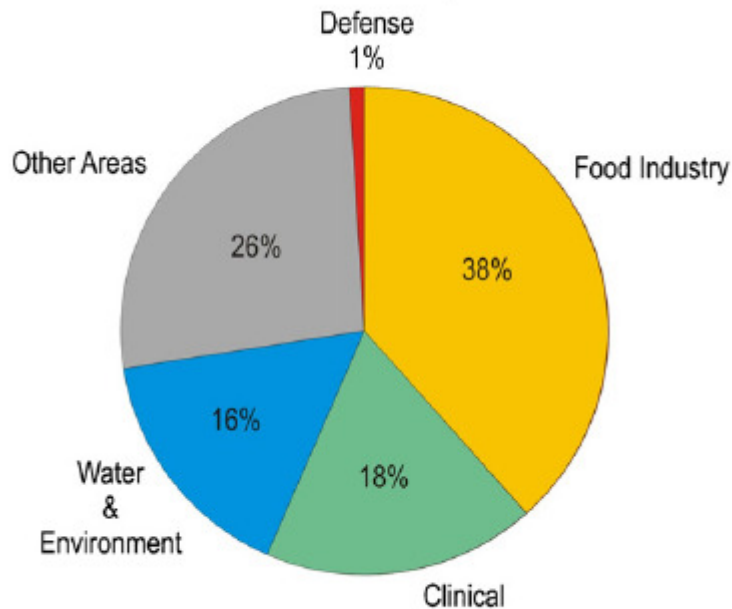


**Figure 1.1 Comparative toxicity of effective doses of biological agents, toxins, and chemical agents[1]**

Bacteria are small, single-celled organisms, most of which can be grown on solid or in liquid culture media. Under special circumstances, some types of bacteria can transform into spores that are more resistant to cold, heat, drying, chemicals, and radiation than the bacterium itself. Most bacteria do not cause disease in human beings, but those that do cause disease act in two differing mechanisms: by invading the tissues or by producing poisons (toxins). Many bacteria, such as anthrax, have properties such as Retained potency during growth and processing to the end product (biological weapon), Long “shelf-life.”, · Low biological decay as an aerosol that makes them attractive as potential warfare agents [1-3].

### Areas of interest for pathogen detection



Source: ISI Web of Science. ca. 2500 Articles found on pathogen detection over the last 20 years.

**Figure 1.2 Distributions, by industry of application, of the relative number of works appeared in the literature on detection of pathogenic bacteria[3].**

Biological agents are effective in very low doses. Therefore, biological agent detection systems need to exhibit high **sensitivity** (i.e., be able to *detect* very small amounts of biological agents). The complex and rapidly changing environmental background also requires these detection systems to exhibit a high degree of **selectivity** (i.e., be able to *discriminate* biological agents from other harmless biological and non-biological material present in the environment). A third challenge that needs to be addressed is **speed** or **response**. One other problem facing the production of biosensors for direct detection of bacteria is the sensitivity of assay in real samples. The infectious dosages of pathogens such as *Salmonella* or *E. coli* O157:H7 is 10 cells and the existing *coli* form standard for *E. coli* in water is 4 cells: 100 ml. Hence, a biosensor must be able to provide a detection limit as low as single *coli* form organism in 100 ml of potable water, with a rapid analysis time at a relatively low cost. Only in this case will the biosensor be convenient

for on-line testing of bacterial pathogens in real samples. Thus, sensitivity is another issue that still requires improvement. There is also a problem of distinguishing between live and dead cells [4-6].

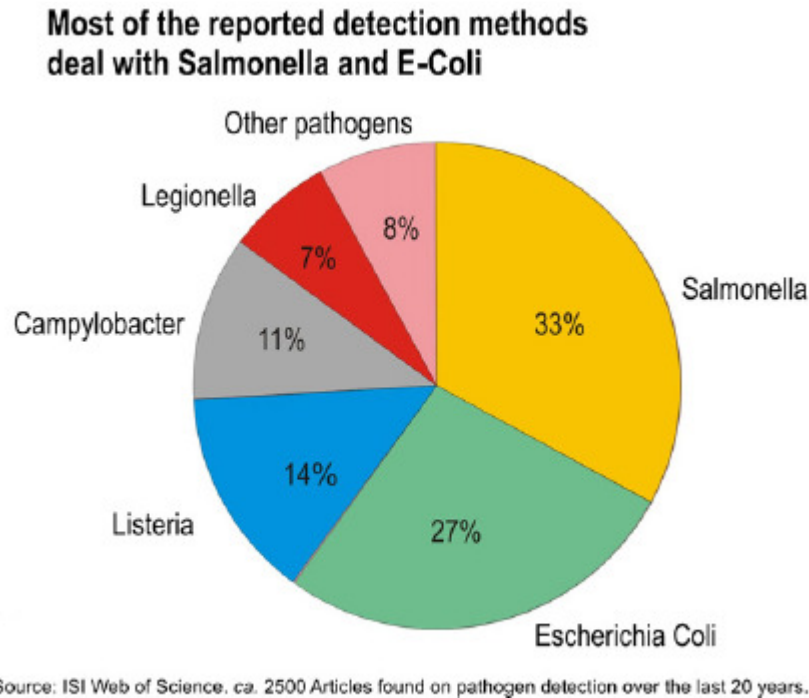


**Figure 1.3 Distribution, by micro-organism, of the relative number of works appeared in the literature on detection of pathogenic bacteria[3].**

These combined requirements provide a significant technical challenge. Additionally, there has been limited development in the area of biological agent detection equipment in the commercial market (i.e., hand-held devices). There are several detection systems being developed and tested by the military that show promise. However, these systems are relatively complicated, require training for successful operation and maintenance, and are expensive to purchase and operate. It is expected that over the course of the next 5 years, commercial instrumentation, hardened for use in the field, may become available at reasonable costs. This eventually leads us to focus our research on developing biological agents' detection techniques

that are very rapid, sensitive and cost effective. Traditionally, infectious agents were detected and identified using standard microbiological and biochemical assays that were accurate but time-consuming. New techniques are needed that combine the accuracy and breadth of traditional microbiological approaches with the improved accuracy and sensitivity[7, 8].

## **1.2. Overview**

The aim of this work is to develop Mass sensors for the detection of biological agents that are hazardous to human life. The current chapter gives the motivation and overview of the organization of study. Next chapter briefs the importance of biosensors and the various types of biosensors that are more emphasized for the detection of biological agents. The various categories are briefly explained with merits and demerits that lead to our research work on the mass sensor made of magnetostrictive strip for the detection process. The chapter also explains the biological pathogen that we focused for our research work and its effects on human life. Chapter 3 portrays the details of the materials and methods involved in the development of the sensor platform. It also includes the theoretical derivation for the determination of the resonance behavior of the sensor due to various mass related distribution conditions. The experimental details also include the numerical specifications and the schematic set up for the detection of the pathogens. Chapter 4 presents the results and discussions of the project describing the factors affecting the resonance behavior of the sensor platform due addition of pathogens as mass and their varsity of distributions. Chapter 5 summarizes the conclusions and potential future work of this study.

## CHAPTER 2

### LITERATURE REVIEW

#### 2.1 Techniques for Pathogens Detection

Amongst the growing areas of interest, the use of rapid methods for defense applications stands out. In fact, the number of publications dealing with these applications already account for over 1% of all publications in the field of rapid methods for pathogen detection since 1985. The food industry is the main party concerned with the presence of pathogenic bacteria. The public health implications of failing to detect certain bacteria can be fatal, and the consequences easily make the news. The following sections describe the various approaches most commonly taken to detect and identify pathogenic bacteria. The uses of biosensors in their most important forms for the detection of pathogens rank fourth among the detection technologies. The percentage of variety of biosensors following transduction method is shown in Figure 2.1[3].

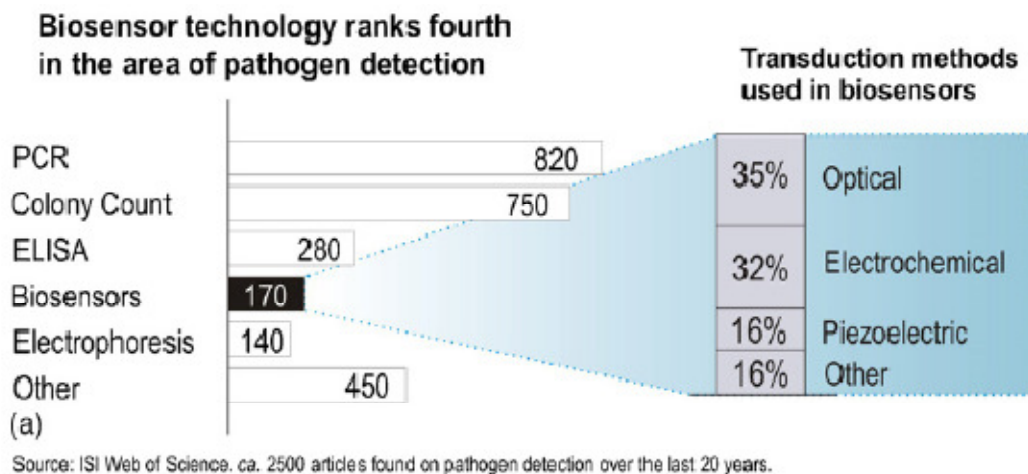


**Figure 2.1** Approximate numbers of articles using different techniques to detect and/or identify pathogenic bacteria[3].

The transducer is the portion of the biosensor responsible for converting the biorecognition event into a measurable signal. As shown in Figure 2.2, it is possible to exploit a change in a number of physical and chemical properties (mass, temperature, electrical properties, and optical properties) to allow for different transduction formats. The four basic transduction types: electrochemical, piezoelectric, calorimetric and optical are reviewed here, with emphasis on the advantages and disadvantages to each, and recent advances toward idealizing biosensor performance[4].

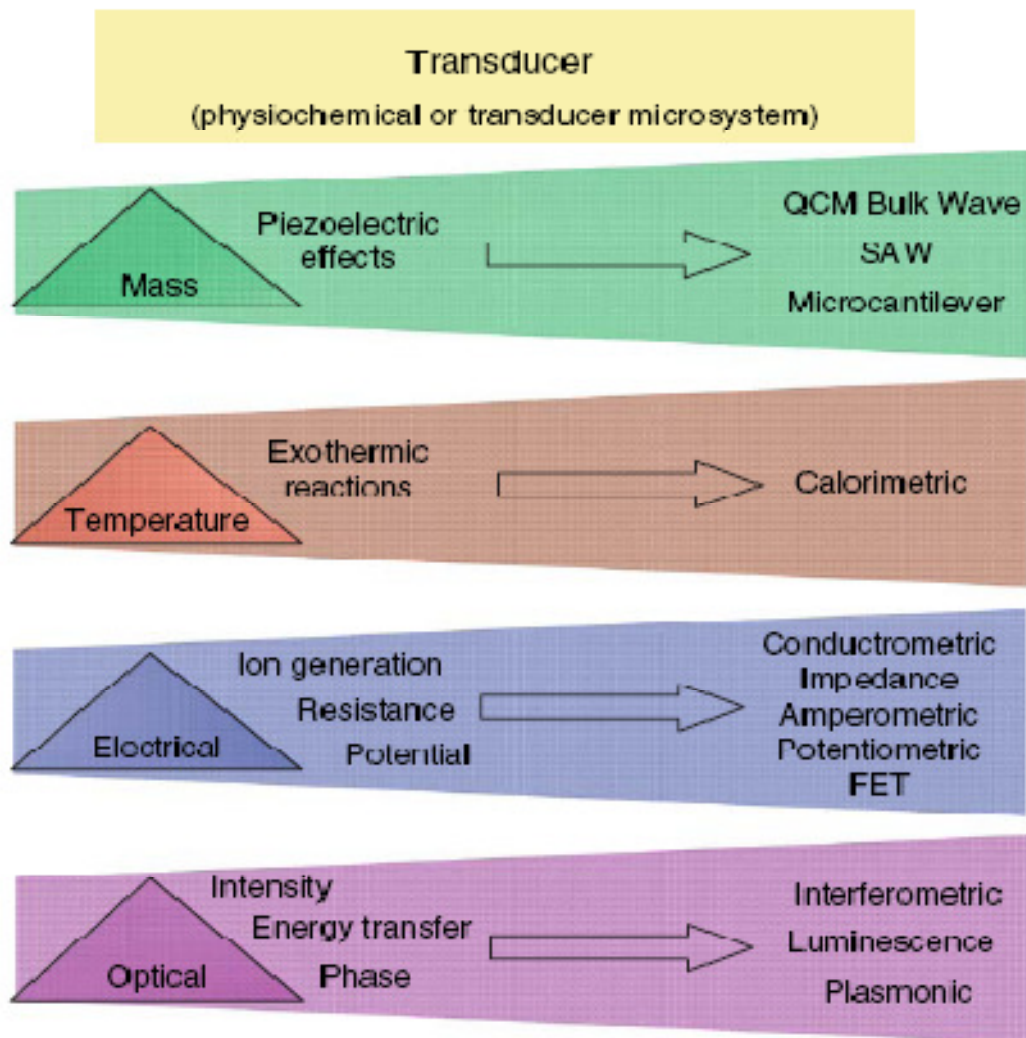


Figure 2.2 Schematic diagram of typical transduction formats employed in biosensors[4].



### **2.1.1 Electrochemical Sensors**

Electrochemical transduction is one of the most popular transduction formats employed in biosensing applications. One of the main advantages of biosensors which employ electrochemical transduction is the ability to operate in turbid media and often in complex matrices. Another distinct advantage of electrochemical transduction is that the detection components are inexpensive and can be readily miniaturized into portable, low cost devices. In general, electrochemical-based sensing can be divided into three main categories, potentiometric, amperometric, and impedance. Potentiometric sensors typically rely on a change in potential caused by the production of an electro active species that is measured by an ion selective electrode. For a biosensor system, this change in electro active species concentration is usually brought about by an enzyme. In an amperometric sensor system, a change in current is directly measured as shown in Figure 2.3. Electrochemical sensors based on impedance, most commonly utilize impedance spectroscopy since controlled AC electrical stimulus over a range of frequencies is used to detect variations in the sensor surface properties (i.e., charge transfer and capacitance at the interface layer). In this way, the resistance to flow of an alternating current is measured as voltage/ current. For example, metabolic changes (e.g., growth and metabolism) have been shown to correspond to an increase or decrease in impedance[6].

Some of the many variations of potentiometric, amperometric, and impedance biosensors that provide for improved biosensor performance include field effect transistors (FETs) and electrochemiluminescence (ECL). Many researchers have recently looked to FETs as a means to miniaturize potentiometric sensors, while providing increased sensitivity due to minimal circuitry. ECL combines the advantages of chemiluminescence (high sensitivity and low

background) with electrochemical transduction. On the other hand, electrochemical methods present slightly more limited selectivity and sensitivity than their optical counterparts

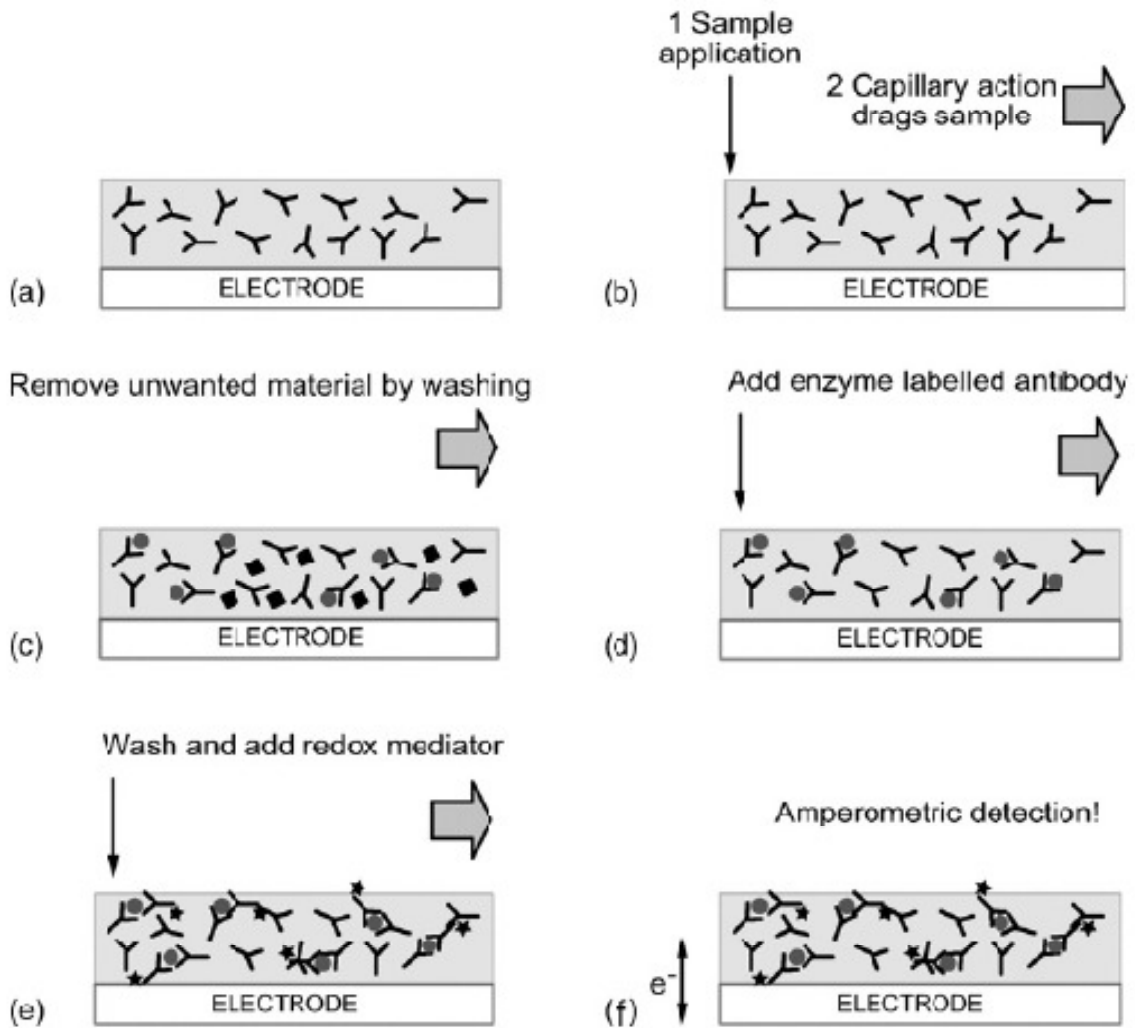
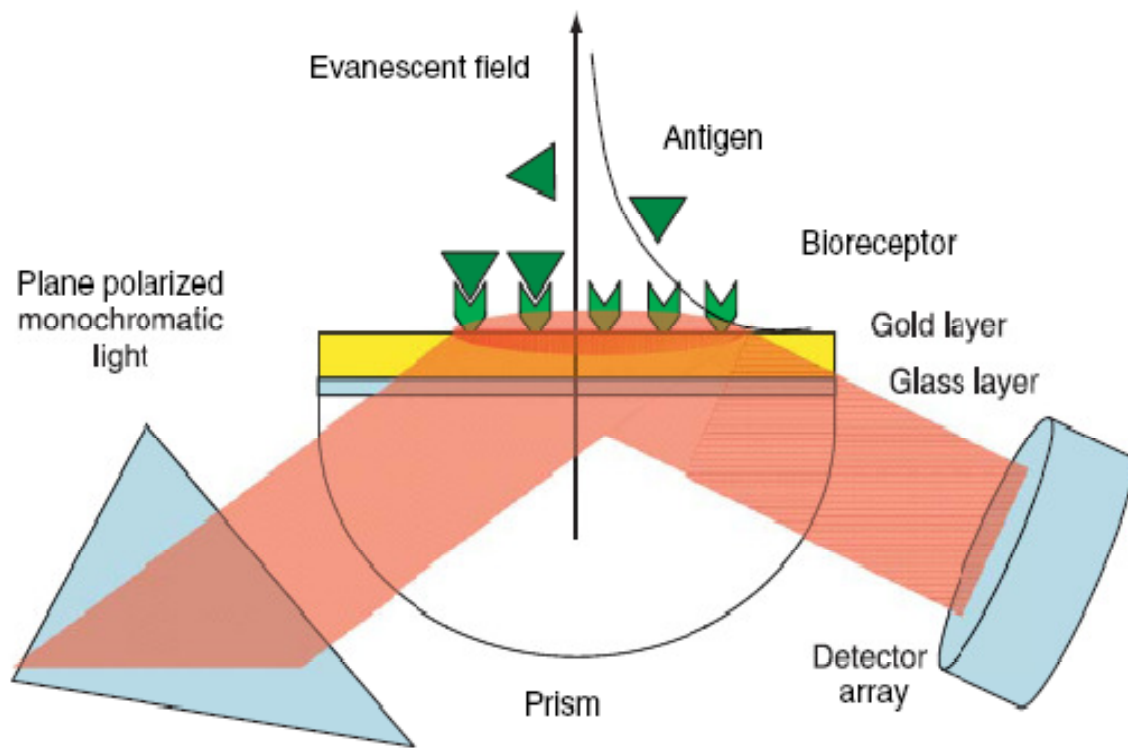


Figure 2.3 Diagram of how an amperometric immunofiltration biosensor works[3].

### 2.1.2 Optical Sensors

Optical biosensors have received considerable interest for bacterial pathogen detection due to their sensitivity and selectivity. Optical- based detection offers large number of subclasses based on absorption, reflection, refraction, dispersion, infrared, Raman, chemiluminescence,

fluorescence, and phosphorescence. However, all the above subclasses require a suitable spectrometer to record the spectrochemical properties of the analyte. The most commonly employed techniques of optical detection are surface plasmon resonance and fluorescence due to their sensitivity. Optical techniques using fiber optics, laser, prism and waveguides are also employed for pathogen detection[2].



**Figure 2.4 Schematic diagram of a biosensor utilizing surface plasmon resonance (SPR) transduction[4].**

Direct fluorescence techniques used for bacterial identification are those in which the natural fluorescent components of the bacterium are examined. All bacteria examined by direct methods must produce or contain some suitable fluorophore. An example of a direct fluorescence method is the identification of *Bacteroides* species by the fluorescence of cells held under an ultraviolet lamp (Slots and Reynolds, 1982). Some species of *Bacteroides* were found not to fluoresce, whereas others emitted fluorescence of characteristic colors. Generally a mixture of fluorescent

metabolic products is detected. In many schemes used in the clinical environment, fluorescence is detected visually while the sample is held under a UV lamp. This approach has the advantages of simplicity, low cost, and rapidity. However, there is at least one major limitation to the utility of direct methods. That is, only those bacteria which contain or produce some fluorescent pigment may be examined. Therefore, the utility of this approach is very limited (Rossi and Warner, 1985). SPR biosensors (Cooper, 2003) measure changes in refractive index caused by structural alterations in the vicinity of a thin film metal surface. Current instruments operate as shown in Figure 2.4. A glass plate covered by a gold thin film is irradiated from the backside by p-polarized light (from a laser) via a hemispherical prism, and the reflectivity is measured as a function of the angle of incidence,  $\theta$ . The resulting plot is a curve showing a narrow dip. This peak is known as the SPR minimum. The angle position of this minimum is determined by the properties of the gold-solution interface. Hence, adsorption phenomena and even antigen-antibody reaction kinetics can be monitored using this sensitive technique (as a matter of fact, SPR is used to determine antigen-antibody affinity constants). The main drawbacks of this powerful technique lay in its complexity (specialized staff is required), high cost of equipment and large size of most currently available instruments. SPR has successfully been applied to the detection of pathogen bacteria by means of immunoreactions (Taylor et al., 2005; Oh et al., 2005a). Optical techniques perhaps provide better sensitivity than electrochemical ones, but their cost and complexity makes them unattractive to most end users[2].

### 2.1.3 Mass Sensors

Biosensors that detect the change in mass due to target and biorecognition element interactions predominately rely on piezoelectric transduction. Piezoelectric transduction relies on an electrical charge produced by mechanical stress, which is correlated to a biorecognition binding event causing a change in the mass on the piezoelectric device. The main advantage to the piezoelectric transduction (i.e., mass sensor) approach includes the ability to perform label-free measurements of the binding events, including real-time analysis of binding kinetics[4].

#### 2.1.3.1 Quartz Crystal Microbalance Sensors

The most commonly employed transducer is the quartz crystal microbalance (QCM), which relies on a bulk wave effect, illustrated in Figure 2.5. A QCM device consists of a quartz disk that is plated with electrodes.

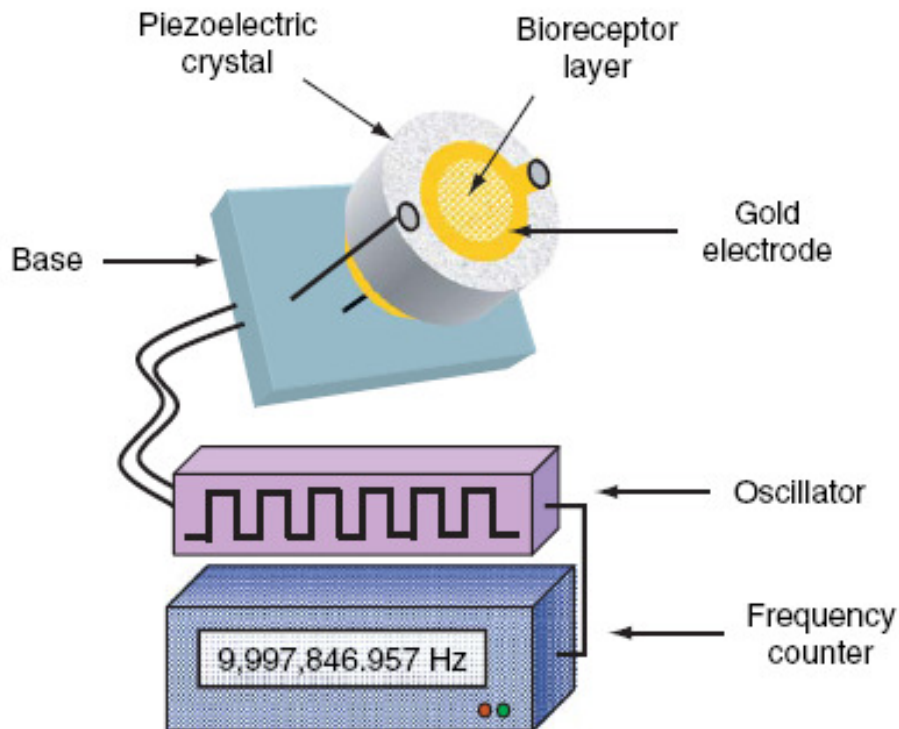


Figure 2.5 Schematic diagram of a biosensor based on piezoelectric transduction[4].

Upon introduction of an oscillating electric field, an acoustic wave propagates across the device. The change in mass associated with bioreceptor–target interactions causes a decrease in the oscillation frequency that is directly proportional to the amount of target. This transduction format can be coupled to a wide variety of bioreceptors (e.g., antibody, aptamer, and imprinted polymer), provided that the mass change is large enough to produce a measurable change in signal. Not surprisingly, QCM transduction is not capable of small molecule detection directly, and usually requires some sort of signal amplification to be employed. A disadvantage of PZ sensors is the relatively long incubation time of the bacteria, the numerous washing and drying steps, and the problem of regeneration of the crystal surface. This last problem may not be important if small crystals can be manufactured at low cost so that disposable transducers are economically feasible. Possible limitations of this technology include also the lack of specificity, sensitivity and interferences from the liquid media where the analysis takes place[9].

### **2.1.3.2 Surface Acoustic Wave Sensors**

Changes in the overall mass of the biomolecular system due to association of the bioreceptor with the target analyte can be measured using alternative piezoelectric transducer devices that offer some advantages over bulk wave sensing. For example, surface acoustic wave (SAW) devices exhibit increased sensitivity compared to bulk wave devices and transmit along a single crystal face, where the electrodes are located on the same side of the crystal and the transducer acts as both a transmitter and a receiver. SAW devices can directly sense changes in mass due to binding interactions between the immobilized bioreceptor and target analytes and

exhibit increased sensitivity compared to bulk wave devices. However, the acoustic wave is significantly dampened in biological solutions, limiting its utility for biosensing applications. Some improvements using dual channel devices, and special coated electrode systems allowing for noncontact SAW devices, which can function in biological solution interfaces have been produced. However, reliable biosensor application incorporating these devices is still under pursuit, as improvements in sensitivity are still required for specific microbial analyses[9].

### **2.1.3.3 Micro cantilever**

An interesting alternative to the optical fiber is the micro cantilever, which measures the presence of substances by non-optical methods. It can act as a physical, chemical, or biological sensor by detecting changes in cantilever bending or vibrational frequency. Think of a diving board that wiggles up and down at a regular interval. This wiggling changes when someone steps on the board. Micro cantilevers are a million times smaller but molecules adsorbed on a micro cantilever cause vibrational frequency changes. Viscosity, density, and flow rate can also be measured by detecting the changes in vibrational frequency. Another way of detecting molecular adsorption is by measuring curling of the cantilever due to adsorption stress on just one side of the cantilever. Depending on the nature of chemical bonding of the molecule, the curling can be up or down. For example, if the micro cantilever is bimetallic, just like the thermostat at home but a million times smaller, a temperature changes as small as a millionth of a degree can be measured. There is much to learn about the basic mechanisms involved.

The micro cantilever is ordinarily constructed of a silicon plank 100 micrometers (mm) long, 30 mm wide, and 3 to 4 mm thick (these dimensions are only approximate, and other geometries are

sometimes used). When molecules are added to its surface, the extent to which the plank bends can be measured accurately by bouncing a light beam off the surface and measuring the extent to which the light beam is deflected. The vibrational frequency can be induced by piezoelectric transducers and measured with the same laser beam that measured the deflection because it generates an alternating current in the detector[10].

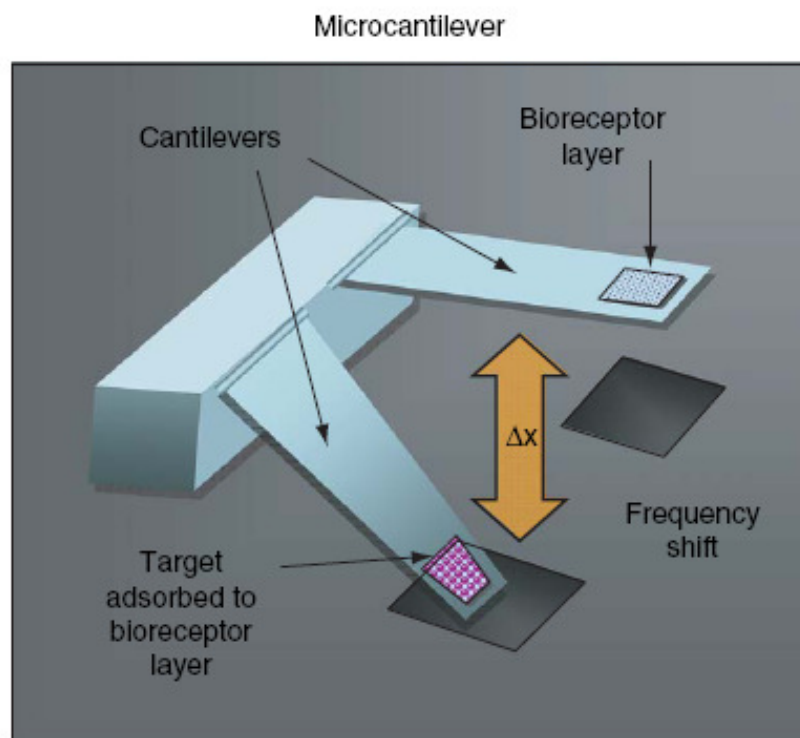


**Figure 2.6 Schematic diagram of a micro cantilever-based biosensor[4].**

Yet another mechanism of response was employed to measure proteins in solution. Antibodies were covalently attached to the silicon surface of a cantilever in such a way that the stresses induced in the antibody when it reacted with its antigen were detected. Detection of biological warfare agents or bacteria and viruses in the hospital laboratory should be expedited with this



stressed antibody technique. Additional experiments are under way to demonstrate the usefulness of the microcantilever as a biosensor.

Because of the small size and versatility of the microcantilever, arrays of sensors can be fabricated on a single chip to conceptually mimic the five sensory facilities: sight, hearing, smell, taste, and touch. ORNL researchers Thomas Thundat, Bruce Warmack, Eric Wachter, Patrick Oden, and Panos Datskos received a 1996 R&D 100 Award for development of the microcantilever[11, 12].

## **2.2 Magnetostrictive Sensors**

Recently, magnetoelastic sensor (ME) platform are gaining attention in chemical and biological sensing. ME sensors are constructed with amorphous ferromagnetic ribbons or wires which are analogous and complementary to piezoelectric acoustic wave sensors. ME sensors are excited with magnetic AC fields and in turn, they generate magnetic fluxes that can be detected with a sensing coil from a distance and hence these sensors are highly attractive for wireless biosensing. They have high tensile strength and are much more cost effective which makes them appealing for biosensor platform. The fundamental operating principle of the magnetoelastic sensors involves a change in sensor resonance frequency due to mass loading of the sensor. In biosensing, the change in mass is associated with the binding of a target analyte to a bioreceptor immobilized on the surface of the ribbon-like ME sensor[13].

The ME sensor can be coated with various probe molecules to target analytes. A change in resonant frequency can be observed if an analyte binds to the magnetoelastic sensor which can be measured rapidly and accurately. Also, the cost of the sensor was approximately is very

cheap, therefore it can be easily utilized as a disposable sensor. Magnetoelastic sensor information is by magnetic flux; hence, no direct connections are needed between the sensor and monitoring electronic equipment making possible a variety of in situ and in vivo monitoring applications. Recently, ME biosensor are developed by immobilizing bacteriophage as biorecognition element for the real-time in vitro detection of *B. anthracis* spores[14].



**Figure 2.7 Magnetostriuctive strips used on valued goods for theft protection**

### **2.2.1 Metglas 2628mb**

Ferromagnetic materials generally are Fe, Ni, and Co metals or their alloys. So far, ferromagnetic materials have been demonstrated to be a good candidate for magnetostrictive sensors because of their soft magnetic properties (low remanence and coercive field) in general. Moreover, ferromagnetic material can be made in amorphous (non-crystalline) metallic alloys by rapidly spinning and cooling of a liquid alloy. For example, Metglas 2826 MB [10], consisting of Fe, Ni, Mo, and B, is a typical amorphous ferromagnetic material having the advantages of nearly magnetic isotropic structure, considerable high permeability, low coercivity, and low

hysteresis loss. Therefore, in this research, we are interested in the ferromagnetic materials including Fe, Ni, Co and their alloys, in particular, Metglas with Fe<sub>40</sub>Ni<sub>38</sub>Mo<sub>4</sub>B<sub>18</sub> in ribbon and sputtered film forms. Metglas 2826 MB is used as the prototype material for fabrication of sensors in bulk-scale and as the sputtering target for deposition of magnetostrictive thin films that are used to fabricate microscale sensor platforms[15]. If a magnetostrictive material is exposed to an alternating magnetic field, it is subjected to compression and extension in the longest axis; subsequently the applied field will be interacted by such a change of inner state of magnetization.

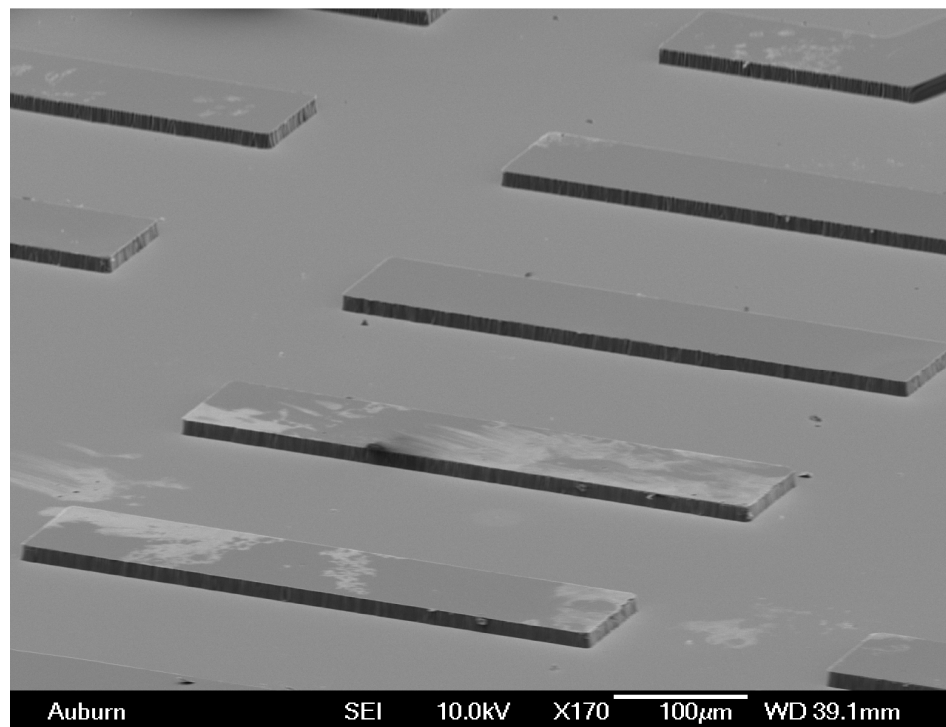


**Figure 2.7 SEM images of the Magnetoelastic strips by simple microfabrication technique.**

When the frequency of the alternating magnetic field is equal to the magnetostrictive material's resonant frequency, the largest oscillation will occur. As a result, the highest magnetic flux density is produced, and the resonant frequency can be detected by analysis of the signal in a

close loop circuit. This is the basis for antitheft sensor tags currently used Electronic Article Surveillance (EAS) system [13, 16] and sensors used to measure chemical and biochemical species. This study will further extend the applications of the magnetostrictive phenomena to detecting mass loaded on magnetostrictive sensors.

### **2.3 Detection of *Escherichia coli*:**

*E. coli* O157:H7 is the source of an estimated 73,000 illnesses, 2,000 hospitalizations, and 60 deaths in the United States every year. The bacterium was first identified by the Centers for Disease Control and Prevention (CDC) in 1975, but was not conclusively determined to be a cause of enteric disease until 1982, following outbreaks of food borne illness that involved several cases of bloody diarrhea. Although most people recover from *E. coli* O157:H7 infection, about five to ten percent of infected individuals develop hemolytic uremic syndrome (HUS), a severe, life-threatening complication of *E. coli* O157:H7 bacterial infection. *E. coli* O157:H7 is responsible for over 90 percent of the cases of HUS that develop in North America[17]. A 7-year-old Cleveland girl died on May 13, 2009 from an *E. coli* infection linked to a massive ground-beef recall. *E. coli* is a potentially deadly bacterium that can cause bloody diarrhea, dehydration and, in the most severe cases, kidney failure. Children, senior citizens and people with weak immune systems are most susceptible to infection[18]. Ong et al. (2006) reported the fabrication and application of wireless, remote-query ME sensors for the quantification of multiple biological agents. A six-sensor array was fabricated for the simultaneous measurement of *E. coli* O157:H7, staphylococcal enterotoxin B, and ricin by immobilizing anti-bacterial or anti-biotoxin antibodies onto a gold-coated ME sensor through self-assembled monolayer

modification cross-linking the antibody with a bifunctional binding agent. The paper reported that the telemetry of magnetoelastic sensor information is by magnetic flux; hence, no direct connections are needed between the sensor and monitoring electronic equipment making possible a variety of in situ and in vivo monitoring applications. Recently, Huang et al. (2008) and Xie et al. (2009) developed a ME biosensor by immobilizing bacteriophage as biorecognition element for the real-time in vitro detection of *B. anthracis* spores[6].

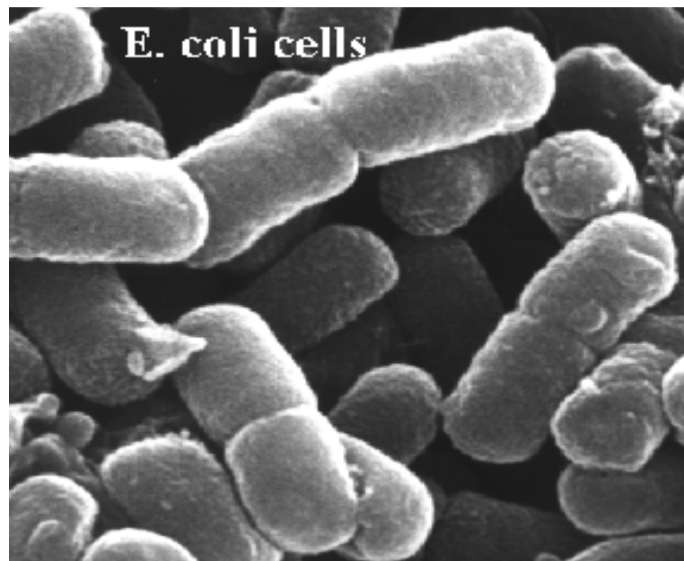


**Figure 2.8 SEM image of *E. coli* O157:H7 cells**

## CHAPTER 3

### MATERIALS AND METHODS

#### 3.1 Magnetostriction

Magnetostriction is the changing of a material's physical dimensions in response to changing its magnetization. In other words, a magnetostrictive material will change shape when it is subjected to a magnetic field. Most ferromagnetic materials exhibit some measurable magnetostriction. The highest room temperature magnetostriction of a pure element is that of Co which saturates at 60 microstrain. Fortunately, by alloying elements one can achieve "giant" magnetostriction under relatively small fields. The highest known magnetostriction are those of cubic laves phase iron alloys containing the rare earth elements Dysprosium, Dy, or Terbium, Tb;  $\text{DyFe}_2$ , and  $\text{TbFe}_2$ . However, these materials have tremendous magnetic anisotropy which necessitates a very large magnetic field to drive the magnetostriction[19].

The mechanism of magnetostriction at an atomic level is relatively complex subject matter but on a macroscopic level may be segregated into two distinct processes. The first process is dominated by the migration of domain walls within the material in response to

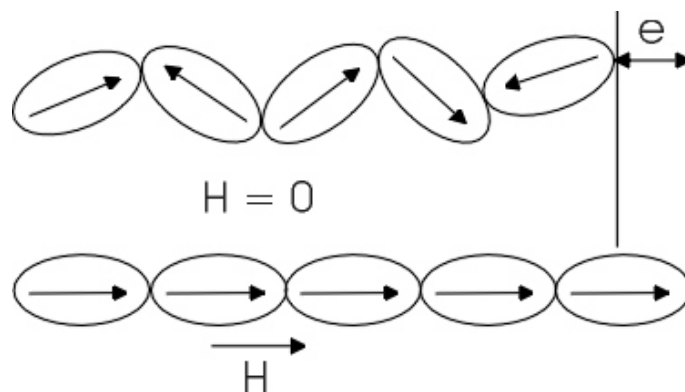


**Figure 3. 2 Schematics of a magnetostrictive sensor's response to the applied magnetic**

external magnetic fields. Second, is the rotation of the domains. These two mechanisms allow the material to change the domain orientation which in turn causes a dimensional change. Since the deformation is isochoric there is an opposite dimensional change in the orthogonal direction. Although there may be many mechanisms to the reorientation of the domains, the basic idea, represented in the figure, remains that the rotation and movement of magnetic domains causes a physical length change in the material[20].

### **3.2 Longitudinal Vibration mode**

The Magnetostrictive materials are fashioned into acoustic wave sensors in the form of simple rectangular strips that are actuated in their longitudinal vibration mode when exposed to magnetic field which is quite different from transverse resonance mode [21-24]. Figure 3.2 illustrates the difference between these two modes for a freestanding beam. When the alternating magnetic field is applied to a sensor that is made of magnetostrictive material in a rectangular shape, with the easy magnetization axis aligned with the longitudinal direction, it can cause the sensor to oscillate in its resonant frequency. Here, the magnetic energy is transferred to mechanical energy to cause the sensor to change its shape (dimension) as a result of switching domains in the magnetostrictive sensor. The strip is simply stimulated with a modulated magnetic field and driven to resonance. A read coil monitors the sensor's magnetic field emissions. Due to the applied field the strips resonate at a specific frequency which is dependent on their mass and physical dimensions[23, 25].

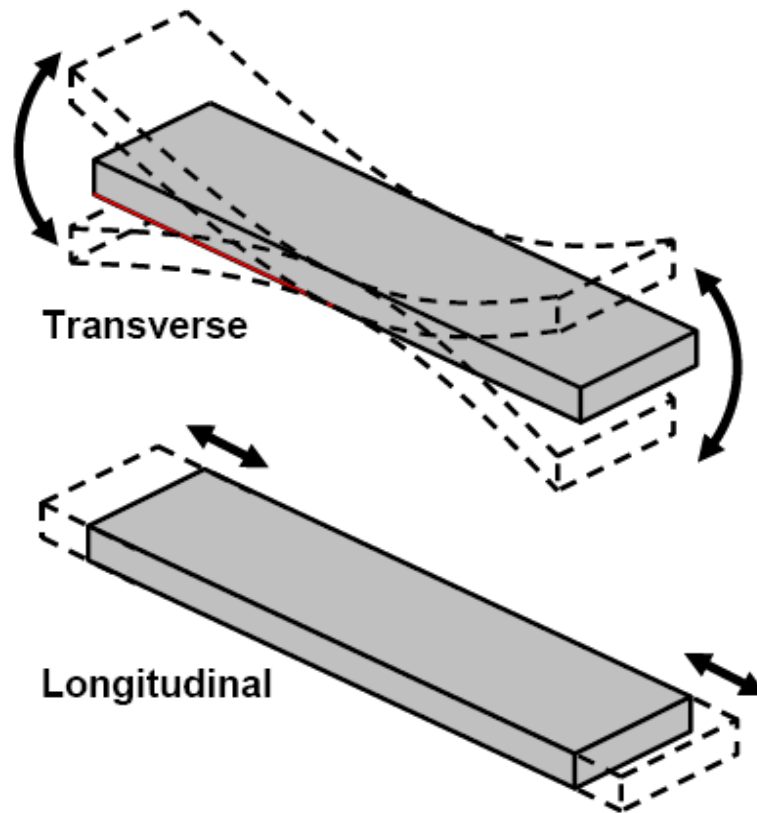


**Figure 3.3 Transverse vs. longitudinal actuation illustrated with a freestanding magnetostrictive strips[26].**

### **3.2 Principle of operation**

In this research, the principle of detection of these sensors involves measuring a resonant frequency shift as the target biological species attaches to the sensor; effectively this addition of mass dampens the resonant behavior of the sensor platform. In the case of monitoring harmful biological agents, it is highly desired to detect the presence of a handful of spores/cells since many harmful agents have a very low pathogenic limit in humans, meaning it only takes a few spores/cells to infect them[27, 28]. When biological agents attach to these magnetostrictive sensors in small amounts they represent discrete mass additions, whereas a large number may be



more analogous to mass evenly distributed on the strip. It is therefore highly desirable to better understand how spore/cell attachment location influences the resonant frequency of these magnetostrictive strips.

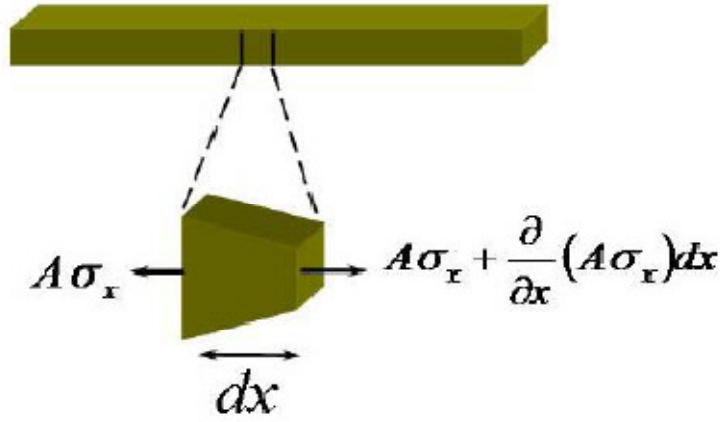


**Figure 3.4 Mechanical force analysis in a unit of sensor[29].**

For a sensor under the magneto-mechanical interaction, a magnetoelastic force is produced in a longitudinal direction, which is  $x$  in this case. The unit mechanical force analysis is explained in Figure 3.3. The total force in the unit is equal to the product of unit mass and acceleration speed base on the Newton's 2<sup>nd</sup> law, as expressed in Equation (3.1)

$$\frac{\partial}{\partial x} (A\sigma_x) dx = m \frac{\partial^2 u}{\partial t^2} \quad (3.1)$$

where  $u$  is the elastic body deformation (longitudinal displacement from the position of equilibrium) in the  $x$  direction,  $\sigma_x$  is the stress in  $x$  direction, and  $\frac{\partial^2 u}{\partial t^2}$  is body deformation acceleration speed. In applying Hooke's law, Equation (3.2), to this, a general equation for a uniform cross section rectangular sensor is then obtained, Equation (3.3)

$$\sigma_x = -E\varepsilon_x = -E \frac{\partial u}{\partial x} \quad (3.2)$$

$$\frac{\partial^2 u}{\partial t^2} = \frac{E}{\rho} \frac{\partial^2 u}{\partial x^2} \quad (3.3)$$

where  $u$  is the elastic body deformation (displacement) in  $x$  direction, and  $\frac{\partial u}{\partial x}$ ,  $\frac{\partial^2 u}{\partial x^2}$  are the strain and strain rate, respectively.  $E$  and  $\rho$  correspondingly denote the Young's modulus and density of the sensor material. Young's modulus  $E$  expressed here is dependent on the state of strain in the structure. The elastic body deformation (displacement)  $u$  should be such a function of  $x$  and (time)  $t$  as to satisfy the partial differential of Equation (3.3).



**Figure 3.5 Schematic of sensor structure in beam.**

When a free-free ended structure sensor thereafter called beam as shown in Figure 3.4, is actuated in the longitudinal vibration mode, the natural frequency can be obtained by applying the boundary conditions of

$$(u)_{x=0} = 0$$

and

$$\left(\frac{\partial u}{\partial x}\right)_{x=L} = 0$$

to Equation (3.3), and the resonant frequency in longitudinal vibration mode without considering the damping effect is obtained as following equation

$$f = \frac{n}{2L} \sqrt{\frac{E}{\rho}} \quad (3.4)$$

Where  $n$  is integral, equals to 1,2,3....., for the first mode,  $n=1$ .  $L$  is the length of the sensor.

The basic sensor structure investigated was a freestanding beam with no fixed ends. The resonance frequency of the first harmonic mode of such a structure can be described with the damping effect is obtained with reference to Cai et. al [25]as,

$$f = \frac{1}{2L} \sqrt{\frac{E}{\rho(1-\nu)}} \quad (3.5)$$

Where,  $L$ ,  $E$ , and  $\rho$  are the length, Young's modulus, and density of the sensor strip, respectively.

As these freestanding magnetostrictive strips are driven to their first harmonic mode, the entire strip deforms in response to the field. The resulting deformation waves propagate through the strip and reflect back from the free ends and cancel at the strip's center, which is the zero nodal position for a freestanding beam resonating in its first harmonic mode[30]. It should be noted that positions further from the center node of the strip move further from the node during deformation due to the accumulated deformations of all positions between it and the node. Thus, the free ends move the furthest. When mass becomes attached to the sensor it effectively dampens the speed of the deformation waves propagating in the strip, which reduces its resonant frequency[14]. The frequency shift as a result of mass attachment for acoustic-based sensors such as these is described the following equation,

$$\Delta f = -\frac{f_0}{2} \left\{ \frac{\Delta m}{m_{sen}} \right\} \quad (3.6)$$

Where  $\Delta m$  is the mass bonded on a sensor,  $\Delta f$  is the resonant frequency change before and after mass attachment,  $m_0$  and  $f_0$  is the sensor's initial mass and resonant frequency, respectively. Here, the bonded mass ( $\Delta m$ ) on the sensor's surface is considered as an evenly distributed mass and is considerably small with respect to the sensor's mass[27]. Accordingly, the change in frequency can be related to the amount of mass bonded on the sensor. However, in the case when a mass is not evenly distributed or is a discrete mass bonded in a particular location this equation is no longer valid. This work will investigate the influence of discrete mass additions, as in the attachment of a target biological species, on the acoustic response of the sensor. In order to study these effects discrete masses were attached at various positions on the sensor and the response was measured and analyzed[31].

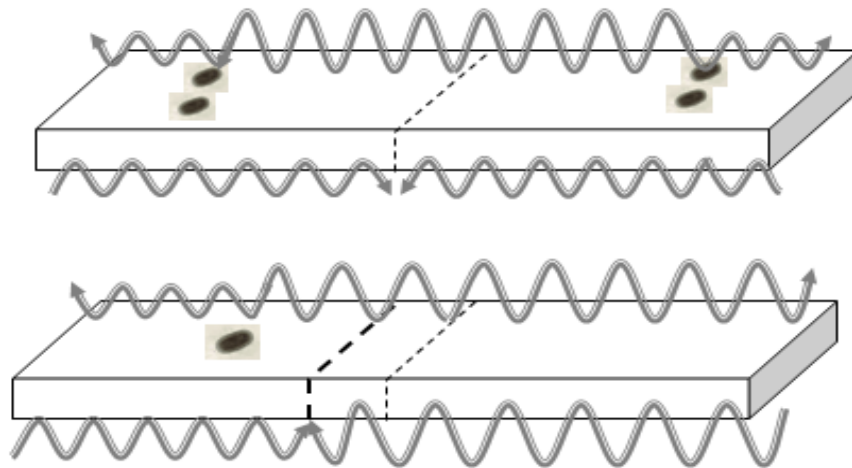


**Figure 3.7 Effect of Mass attachment on the wave speed of the sensor platform due to longitudinal vibration.**

### 3.3 Design and Numerical Simulation

Numerical simulations were carried out using commercially available software Ansys®. Specifically, the simulations involved modal analysis on an undamped, freestanding beam with oscillations in the longitudinal mode both with and without attached mass. The structural physical (engineering) discipline is preferred for the Modal analysis of Magnetostrictive sensors. The selected element type was SOLID186, The sensor size employed here was  $250 \times 50 \times 4 \mu\text{m}$ , and the attached mass were representative of an actual *E. Coli O157:H7* cell, size of  $1.43 \times 0.73 \times 0.73$  microns and weight of 1 picogram[12].

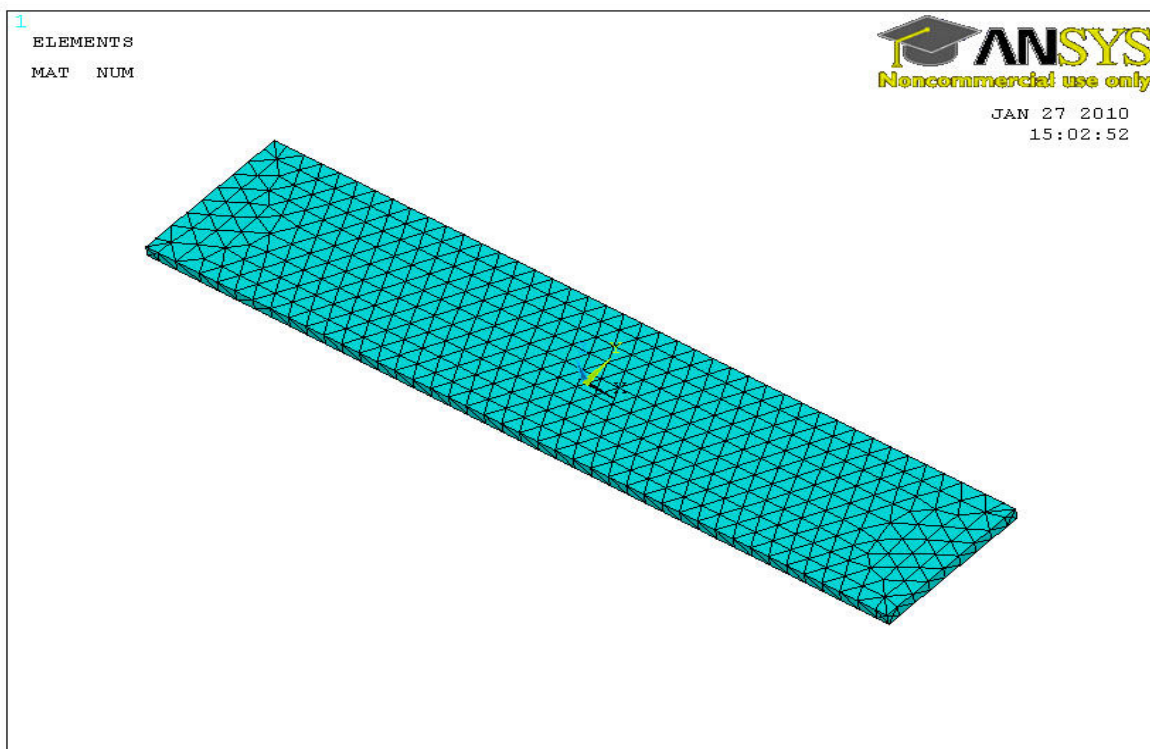


**Figure 3.8 Simulation result of a  $250 \mu\text{m} \times 50 \mu\text{m} \times 4 \mu\text{m}$  sensor meshed with tetrahedral facets of element size  $7.5 \mu\text{m}$ .**

The sensor platform was meshed with the element type tetrahedral facets of size 7.5  $\mu\text{m}$  by smartsizing option in the mesh tool as shown in Figure 3.6. The boundary conditions were set to obtain longitudinal vibration mode of the sensor platform.

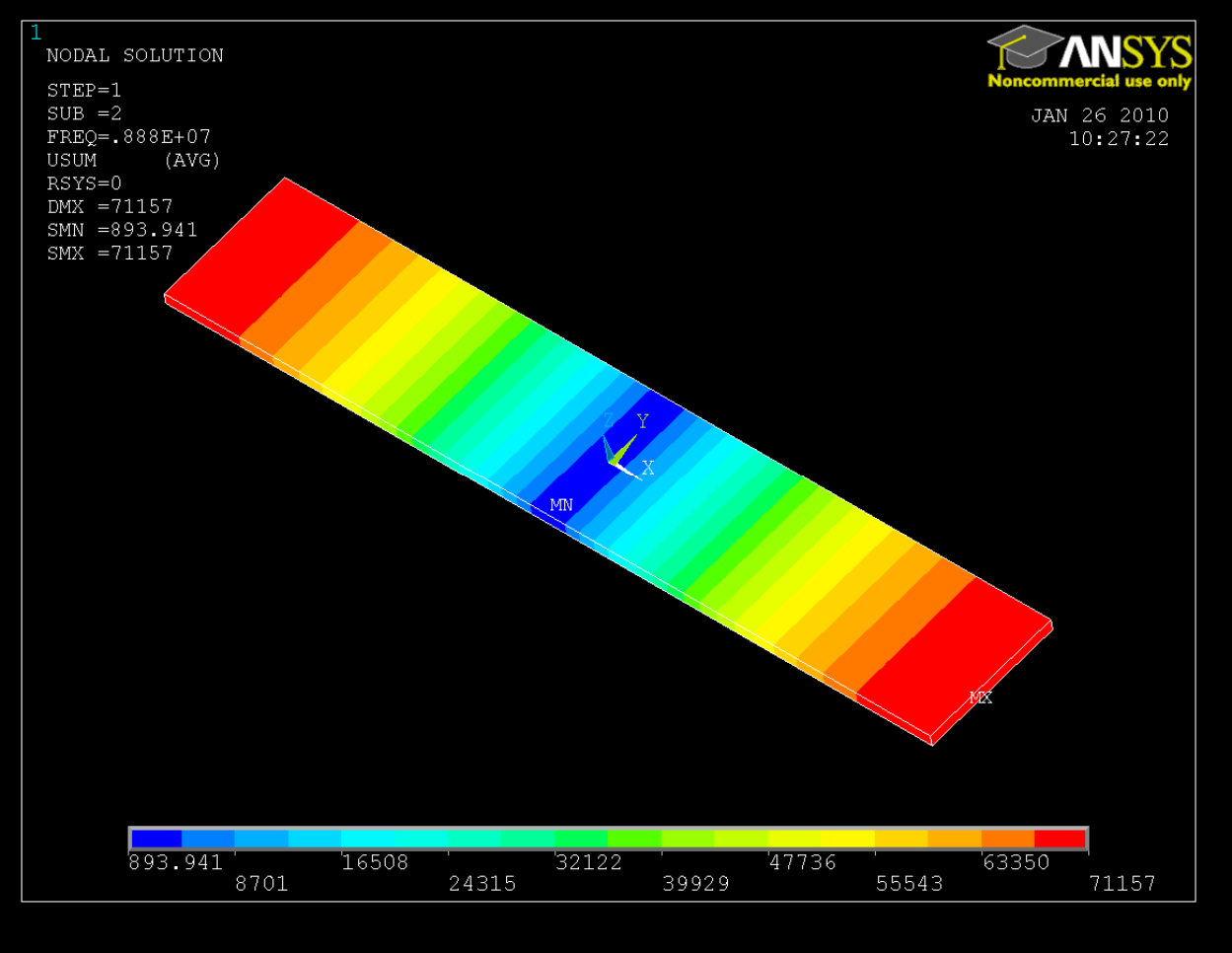


**Figure 3.9 Simulation results for freestanding Metglas beam with the size of 250  $\mu\text{m}$  x 50  $\mu\text{m}$  x 4  $\mu\text{m}$ . Poisson’s ratio of 0.33 was employed.**

Figure 3.7 shows the sensor model with the range of deformation denoted by varying colors. Red color on the free ends of the platform show the maximum deformation and blue color at the centre depicts the minimum deformation obtained due to the longitudinal vibration mode of the

sensor platform. The simulation figure also provides the resonant frequency of 8.8753 MHz for the default sensor dimension  $250 \times 50 \times 4 \mu\text{m}$  used throughout our research work considered to be  $f_0$ . Prediction model was developed involving the factors influencing the resonance behavior such as (a) Mass distribution, (b) Position of the mass distributed and (c) Physical dimension of the sensor platform in compliance with the theoretical equations and simulation results. Mass of *E. coli* cells were distributed as a single layer for uniform distribution. The later was glued to the sensor platform and subjected to numerical simulation with the application of boundary condition over the whole setup. The density of the layer was modified each time for different amount of mass in uniform distribution case and the corresponding variation in frequency shift was observed. In case of the non uniform distribution the layer was split and concentrated along the free ends gradually moving towards the central nodal line and vice versa[23].

### **3.4 Experimental Method**

Thin films of Au, Cu, Al, Cr, In, and Sn were DC sputter deposited onto a sensor cut from Metglas ribbon (smooth side) by a Discovery 18 sputter system from DENTON VACUUM, Inc. All targets were purchased from Kurt J. Lesker, Inc. with purity of 99.99% or better. The SiC thin film was obtained by directly sputtering from a SiC target with Ar plasma. More details can be found in Liang et al. [26]. The background vacuum was achieved at  $3 \times 10^{-6}$  torr or better for each deposition. Sputter power density of  $4.5 \text{ w/cm}^2$  was used for the metallic films deposition, and a Ar flow rate of 25 sccm with the process pressure of 5 mT were employed for all sputtered films. A thin layer of 12 nm Ti was applied by RF sputter as an adhesion promoter prior to Cu or Au film deposition without breaking the vacuum. An Au rich lead-free solder AuSn (80/20 wt. %) thin film was obtained by co sputtering of Sn and Au targets, simultaneously. A deliberated

experiment was performed to obtain the correct composition of AuSn (80/20) eutectic solder, which was examined by EDX. All targets were sputter cleaned for 15 minutes with shutter covered before deposition. Thin film thickness was controlled by sputtering time and measured by a TENCOR alpha-step 200 profilometer from TENCOR Instruments, Inc. A Rigaku X-Ray Vertical Diffractometer with Cu K $\alpha$  radiation was employed to characterize the crystal structure of these thin films, and the surface morphology of the film was characterized by using a JEOL JSM 7000F field-emission SEM equipped with EDX capability. Metglas 2826 MB ribbon was obtained from Metglas, Inc. and cut to sizes of 8 mmx1.6mm by a semiconductor ranked dicing saw and cleaned with acetone, methanol, IPA(Isopropyl Alcohol), DI (deionized) water and dried by nitrogen gas. The sensors were dehydrated in a convection oven at 120°C for 20 minutes prior to use[29].

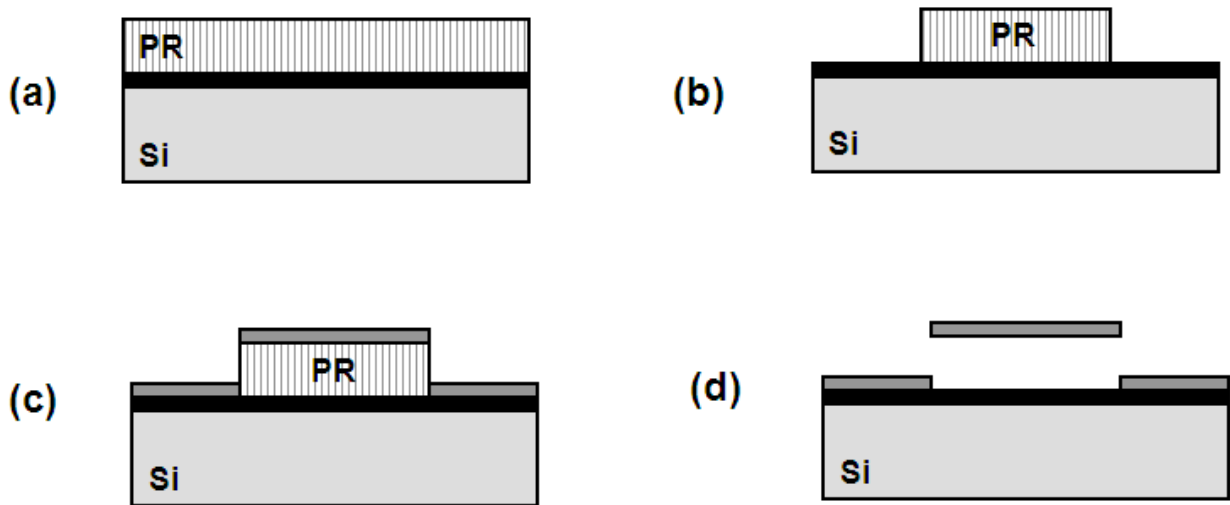


**Figure 3.10 Procedural steps involved in the Microfabrication of Magnetostrictive strips for the sensor platform.**



### 3.4.1 Glass beads attachment

Sensors with dimensions of 5 mm length and 1 mm width were cut from a 28  $\mu\text{m}$  thick commercially available Metglas 2826MB strip[15]. These specimens were prepared, by cleaning and drying, using the identical procedures described by the authors elsewhere. Glass beads with a diameter about 425  $\mu\text{m}$  were employed to simulate the concentrated mass and were carefully loaded on to the sensor surface at prescribed locations and secured with adhesive. The average mass of a sensor and glass bead were 1066  $\mu\text{g}$  and 181.5  $\mu\text{g}$ , respectively.

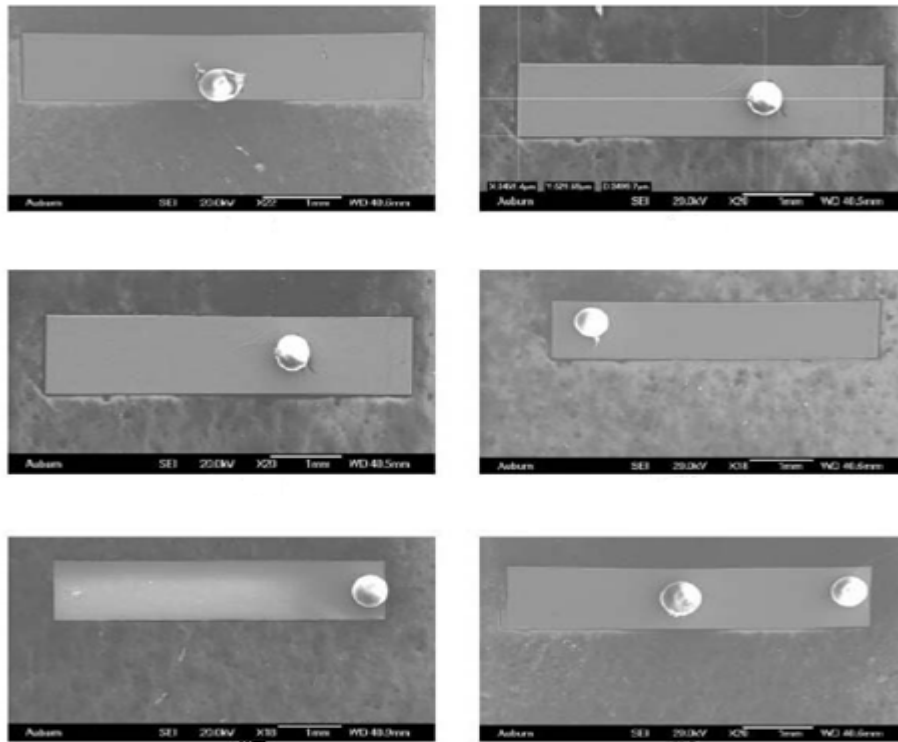


**Figure 3.11 SEM images showing glass beads attached to the sensor in various locations.**

It should be noted that these experiments are aimed as assessing the position of the mass concentrations and not focused on demonstrating minimum sensitivity. Thus, significantly sized beads were employed as shown in Figure 3.9. The amount of glue employed to affix each bead

as well as its position were well controlled to minimize any errors. After a glass bead was loaded on the sensor surface, it was immobilized by drying at room temperature for at least two hours. The resonant frequency of the sensor was measured before and after attachment of the glass bead in a manner identical to which is discussed in previous work by the authors [5, 32-34].

### 3.4.2 Detection Setup

The test setup consists of three key units, a HP8751A network analyzer (a), a custom made read coil that serves as a A/C magnetic field generator and sensor's signal pick up (b), and a permanent magnetic bar that serve as a magnetic bias field (c), as shown in Figure 3.4. Note that the read coil is directly connected to port 1 of the network analyzer and both the read coil and magnetic bar are not in scale. They are enlarged for better observation.

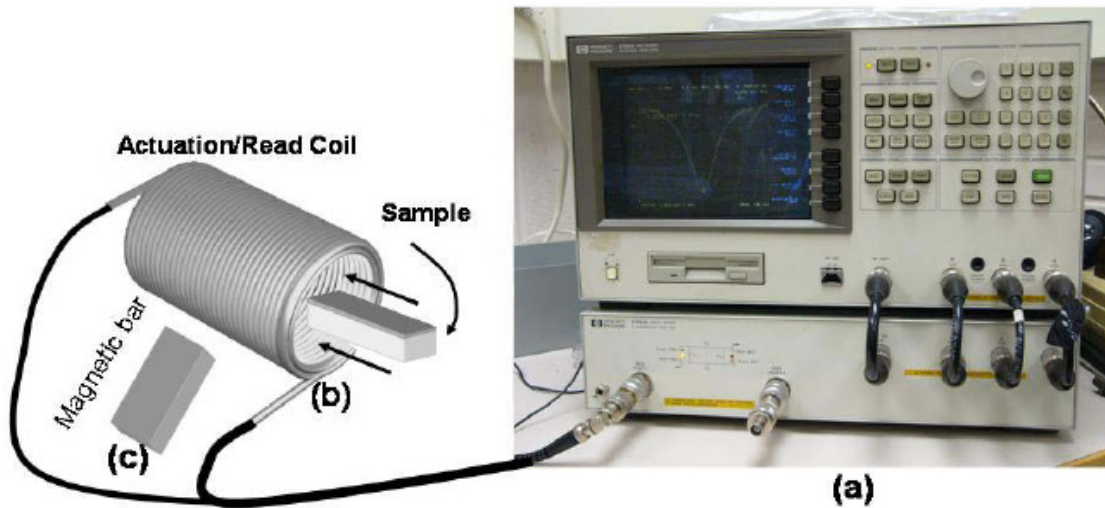


**Figure 3.12 Resonant frequency detection setup containing Actuation/read coil, and magnetic bar**

The characteristics of a magnetostrictive sensor can be characterized through this set up. The basics can be described as follows: when the analyzer sends a RF swept signal (exciting signal) or power, through the coil, which generates an A/C magnetic field in the coil, a magnetostrictive sensor inside the coil will alternatively change its shape or vibration as a result of response to this A/C magnetic field. Such change in shape of the sensor will produce a second; an alternative magnetic field that will interact with the read coil (also called pick up) to generate a second, an alternatively signal at the same frequency as the applied RF signal. When the frequency of the applied RF swept signal reaches the resonant frequency of the magnetostrictive strips, oscillation occurs, and the strips are deformed, therefore, reaching its maximum. Consequently, this is the largest interaction between the magnetostrictive strips and the pick-up coil. This largest interaction results in the largest power change in the device under test (DUT) and network, which is analyzed by the network analyzer through measuring either the transmitted or the reflected signal[29].

## CHAPTER 4

### RESULTS AND DISCUSSION

#### 4.1 Distribution of Mass

There are several ways of distributing the mass over the sensor platform. In this research work we carried out the simulation part by distribution mass over the sensor platform using Boolean operation which glues the *E.coli* cells onto the sensor platform. This process was done with the assumption that no two *E.coli* cells can accumulate to the sensor platform in one over the other format which means cells were individually glued to the sensor platform directly.

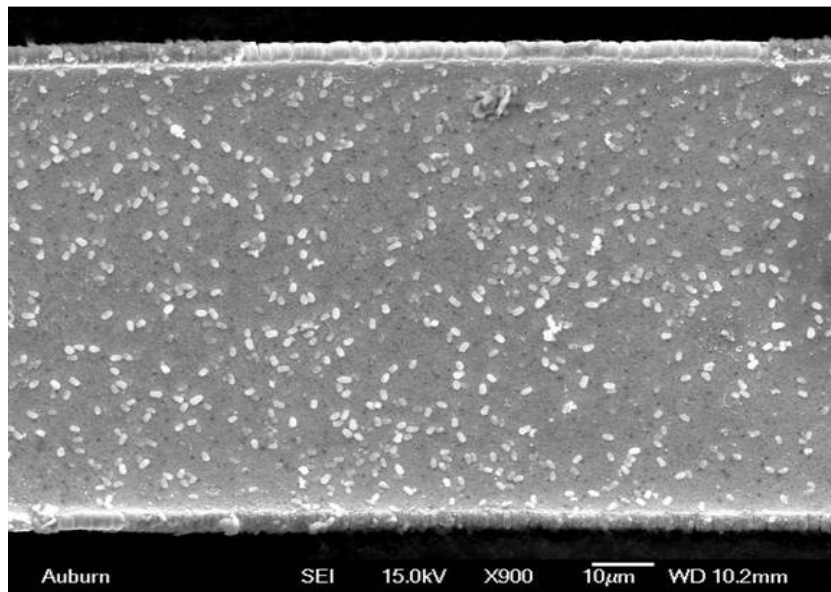


**Figure 4.1 SEM image of the sensor platform with the uniform distribution of *E.coli* cells attached experimentally.**

This assumption was carried on based on the experimental work described in Guntupalli, et al. and Wan, et al. both demonstrated that the density of bonded spores/cells on this type of sensor changed as a function of spore/cell concentration (on the order of  $10^5$  to  $10^9$  CFU/ml) as shown

in Figure 4.1. Other observations in these papers included that the uniformity of bonded spores/cells decreased when spore/cell concentration decreased and that there was a significant discrepancy between the number of bonded spores/cells experimentally observed and theoretically predicted on the surface. This is because the bacteriophage they use to immobilize the sensor platform can hold one cell per phage and that would limit the number of cells attached to the sensor platform.

#### 4.1.1 Uniform Distribution

In case of Uniform distribution simulations were carried out by varying the density of the layer that was glued to the sensor platform beginning with actual density of the *E.coli* cell followed by decreasing the density upto a certain level. Accordingly we could notice a linear decrease in the frequency shift due to reduction in density. This basically is carried out in a way that the cells are distributed uniformly over the platform and also we managed to reduce the number of cells in a gradual way.

**Table 4.1 Resonant Frequency shift due to uniform distribution of *E.coli* cells over the sensor platform**

No of <i>E.coli</i> cells	$\eta$	$\Delta f_{sim}$ (KHz)	$\Delta f_{cal}$ (KHz)
0	0	0	0
1197	0.00303	12.8	13.4
2281	0.005775	25.0	25.7
4563	0.011552	50.6	51.4
6844	0.017327	76.1	77.1
9125	0.023101	102	102.8
11974	0.030314	134	135.0

Considering the upper surface of the sensor platform we notice from the Table 4.1 shown below that the maximum possible number of cells were 12000. The cells count was reduced gradually and we can see the corresponding decrease in the frequency shift. Figure 4.2 shows the linear frequency shift of the sensor due to uniform distribution of mass. The straight dark line represents the calculated value for the corresponding number of cells using the Equation (3.7). The square dots were the simulated result values obtained following the boundary conditions and other required specifications for the modal analysis of the sensor in Ansys.

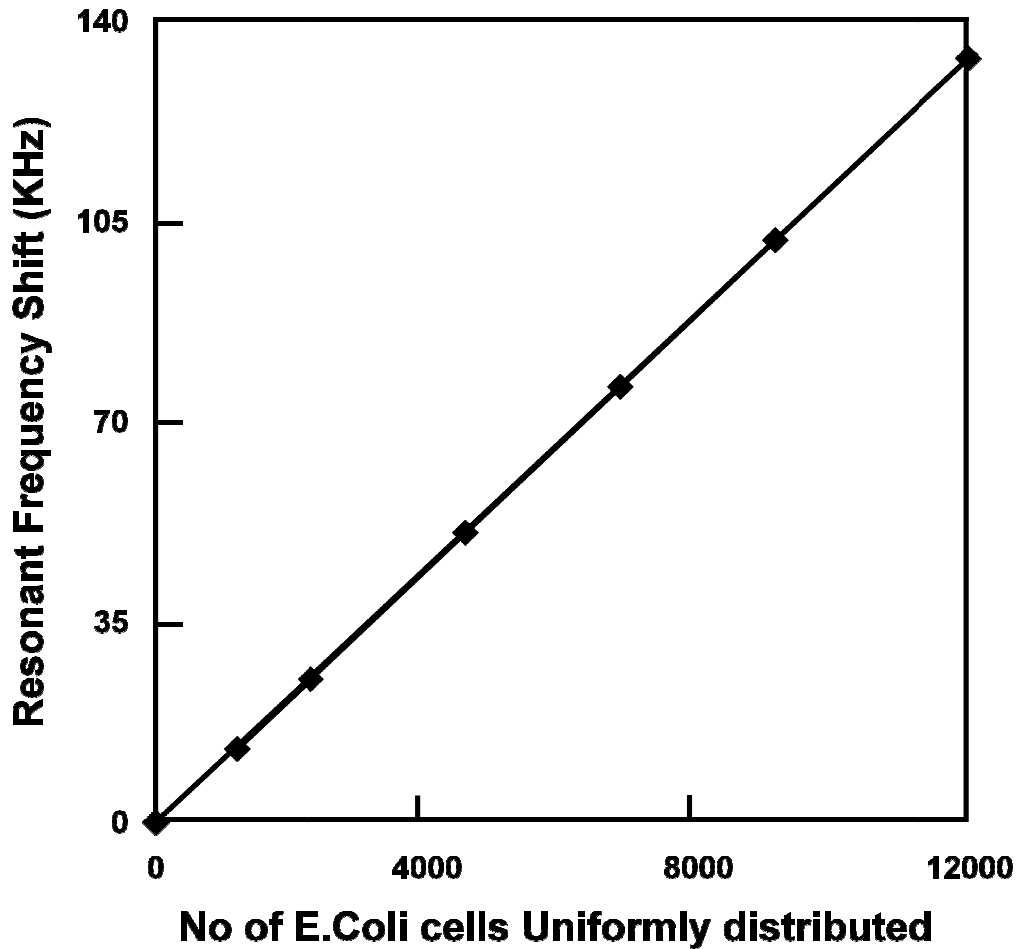
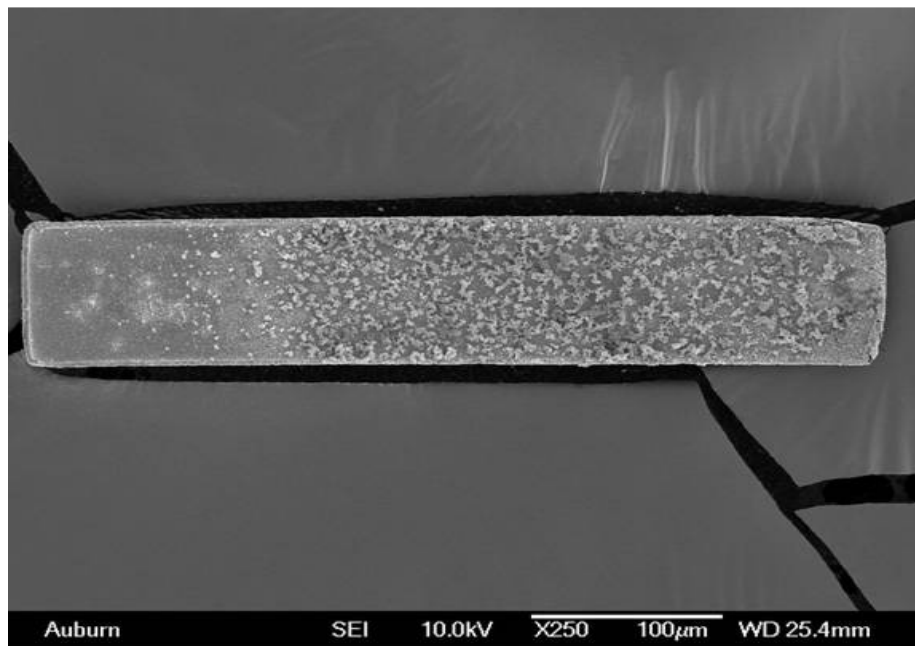


Figure 4.2 Resonant Frequency Shift due to uniform distribution of *E.coli* cells

### 4.1.2 Non-Uniform Distribution

Frequency shift is not the same if the mass is concentrated at a particular location on the sensor platform compared to the uniform distribution of the mass. This is mainly due to reduction in wave speed of the sensor obstructed by the concentrated mass at discrete locations on the platform. There are different ways of placing the pathogens over the sensor platform that would affect the frequency shift of the sensor platform. Our aim in this research work is to determine the tolerance limit of the frequency shift observed by the sensor platform due to the discrete addition of mass at random positions as shown in Figure 4.3.



**Figure 4.3 SEM image of a sensor with Non-Uniform distribution of *E.coli* cells**

The Non-uniform distribution of the mass was carried out by placing layers of varying length over the sensor platform and subjecting it to longitudinal vibration by modal analysis following the same boundary conditions that was applied for the earlier stage of the research work. In this section we are going to deal with two extreme cases of mass distribution and determine the

tolerance limit with the help of the simulation results. To uphold the simulation results we have theoretical derivations and corresponding mathematical calculations.

#### 4.1.2.1 Maximum Frequency Shift

Maximum Frequency shift would be observed when mass is attached at the free ends of the freestanding beam subjecting it to longitudinal vibration mode. For the simulation purpose the mass was non-uniformly distributed in layers as shown in Figure 4.4 till the sensor platform is completely filled with the *E.coli* cells attached over the surface.

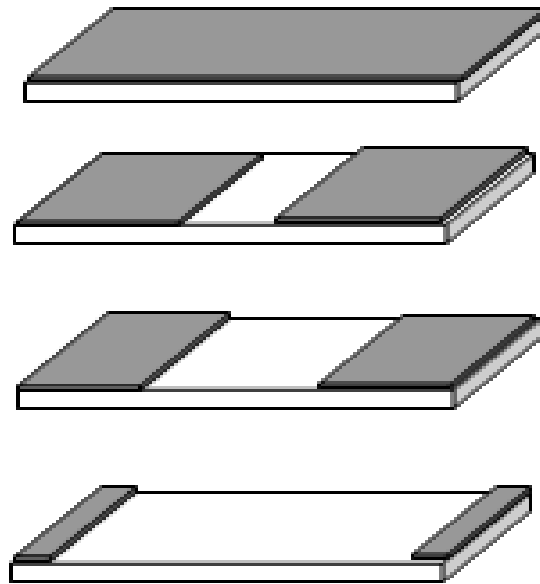


**Figure 4.4 Schematic diagrams representing the non-uniform distribution for the maximum resonant frequency condition**



In such cases theoretical verification could be carried out assuming the boundary conditions will be

at  $x=0$ ,

$$\frac{\partial u}{\partial x} = 0 \quad (4.1)$$

and at  $x=L$ ,

$$\frac{\partial u}{\partial x} (-AE) = \Delta m \left\{ \frac{\partial^2 u}{\partial t^2} \right\} \quad (4.2)$$

Assuming that the beam performs one of the principal modes of vibration, the  $u$ , therefore, can be expressed as a function of  $x$  and  $t$  in Equation (4.3)

$$u(x, t) = f(x)[A \cos(\beta t) + B \sin(\beta t)] \quad (4.3)$$

in which  $A$  and  $B$  are constants,  $f(x)$  is a certain function of  $x$  alone, and  $\beta$  is the angular frequency of this vibrating system. Submitting Equations (4.3) to Equation (4.2), we obtain:

$$f''(x) + \frac{\beta^2 \rho}{E} f(x) = 0 \quad (4.4)$$

The boundary conditions of Equations (4.1) and (4.2), therefore, become

$$f(0) = 0 \quad (4.5)$$

and

$$f'(L) - \left\{ \frac{\Delta m}{EA} \right\} \beta^2 f(L) = 0 \quad (4.6)$$

Let  $\eta$  be the ratio of the attached mass ( $\Delta m$ ) to the mass of the cantilever ( $m_{\text{sen}} = AL\rho$ ), and inserting

$$\eta = \frac{\Delta m}{m_{sen}} = \frac{\Delta m}{AL\rho}$$

into Equation (4.6), we have

$$f'(L) - \eta L \left\{ \frac{\rho\beta^2}{E} \right\} f(L) = 0 \quad (4.7)$$

Thus the standard solution for Equation (4.4) is

$$f(x) = C \cos \left( \beta \sqrt{\frac{\rho}{E}} x \right) + D \sin \left( \beta \sqrt{\frac{\rho}{E}} x \right) \quad (4.8)$$

To satisfy the boundary condition:  $f(0) = 0$ ,  $C$  must vanish and  $\beta$  must be real. Equation (4.8) therefore becomes

$$f(x) = D \sin \left( \beta \sqrt{\frac{\rho}{E}} x \right) \quad (4.9)$$

To meet the boundary condition of Equation (4.7), Equation (4.8) becomes

$$\cos \left( \beta L \sqrt{\frac{\rho}{E}} \right) = \eta \left( \beta L \sqrt{\frac{\rho}{E}} \right) \sin \left( \beta L \sqrt{\frac{\rho}{E}} \right) \quad (4.10)$$

$$\eta \left\{ L \beta \sqrt{\frac{\rho}{E}} \right\} = -\tan \left\{ L \beta \sqrt{\frac{\rho}{E}} \right\}$$

Where

$$K = \beta \sqrt{\frac{\rho}{E}}$$

$$\eta(KL) = -\tan(KL) \quad (4.11)$$

If there is no concentrated mass attached ( $\eta = 0$ ),  $kL$  must be  $0, \pi, 2\pi, 3\pi\dots$ , to satisfy Equation (4.11), therefore, the resonant frequency for this free-free ends system is

$$f = \frac{\frac{n\pi}{L} \sqrt{\frac{E}{\rho}}}{2\pi} = \left( \frac{n}{2L} \sqrt{\frac{E}{\rho}} \right)$$

Where  $n=1,2,3\dots$

If  $\eta$  is infinitely large, the solution to Equation (4.11) is  $kL = \pi/2, 3\pi/2, 5\pi/2$ , and the resonant frequency of this system is

$$f = \frac{\frac{(2n-1)\pi}{2L} \sqrt{\frac{E}{\rho}}}{2\pi} = \frac{(2n-1)}{4L} \sqrt{\frac{E}{\rho}}$$

In such cases the Maximum resonant frequency shift will be observed at the free ends of the sensor platform which can be determined by numerical calculations using equation

$$\Delta f = f_o \left\{ \left( \frac{kL}{2\pi} \right) - 1 \right\} \quad (4.12)$$

Finite element simulations were carried out as shown in Figure 4.3 following the boundary conditions as explained in the experimental methods section.

**Table 4.2 Calculated values of  $\eta$  and KL with the corresponding resonant frequency shift values determined using the Equation (4.12) and (3.6)**

$\eta$	0	0.0005	0.005	0.01	0.05	0.5	1	$\infty$
KL	$\pi$	3.1400225	3.125965	3.110498	2.99304	2.28893	2.02876	$\pi/2$
$\Delta f_{max}$ (KHz)	0	4.452	44.312	88.168	421.205	2408.853	3155.378	4437.650
$\Delta f_{uni}$ (KHz)	0	2.226	22.269	44.539	222.695	2218.825	4437.650	$\infty$

The mass of pathogen was not uniformly distributed as a layer that gradually increases from the free ends to cover the entire sensor platform leading to uniform distribution case. Table 4.2 lists the solution of kL value for Equation (4.12) and the relative resonant frequency shift for some particular  $\eta$  values.

If there is no concentrated mass attached on the end, there is no frequency change. If the attached mass is infinitely large, the resonant frequency is reduced to the half of that for the free-free ended beam system. It can be seen that the relative frequency shift for a concentrated mass attached to one end of the freestanding beam is also higher than that of evenly distributed mass on the sensor surface.

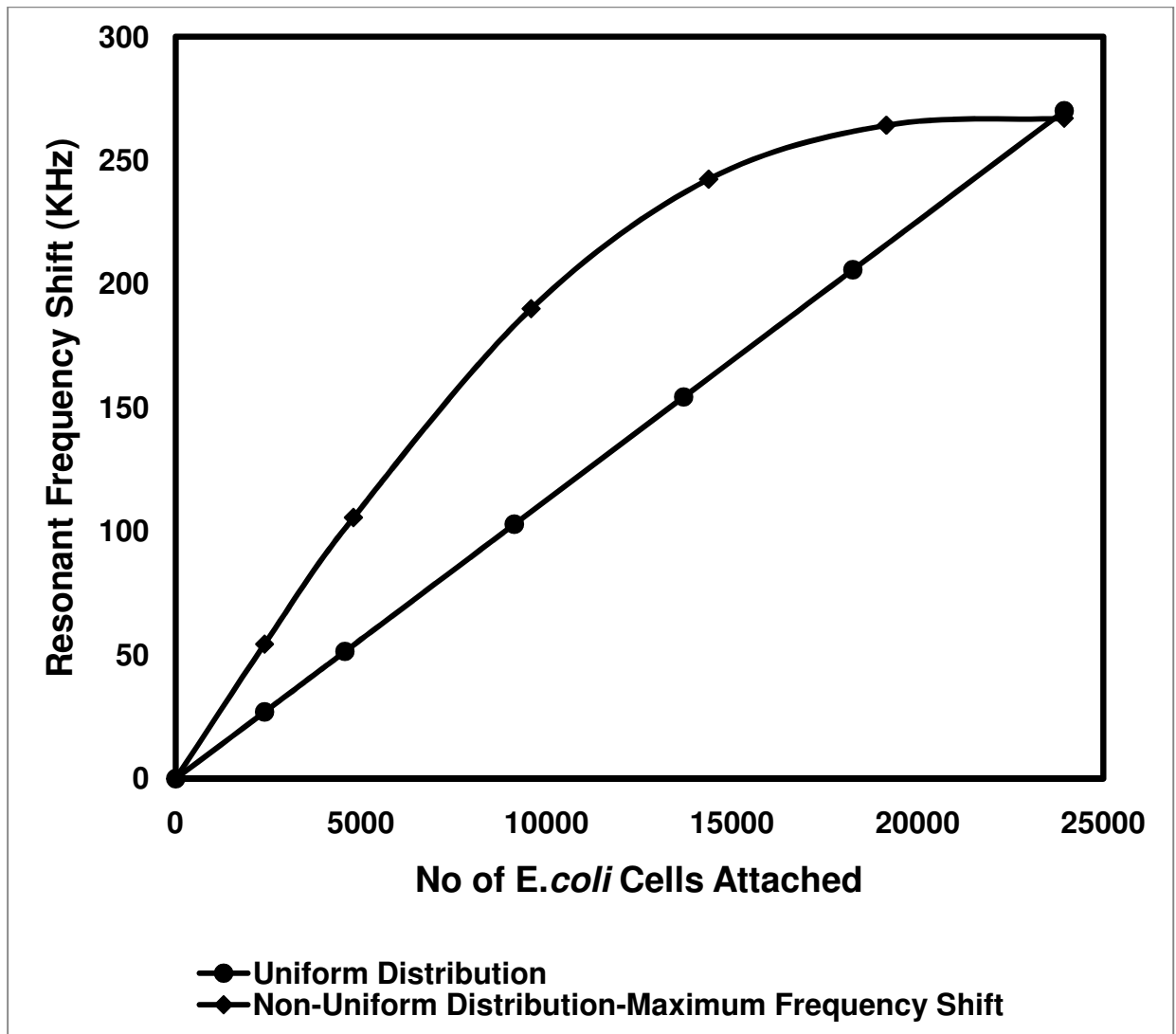


**Figure 4.5 Plots representing the Maximum Resonant Frequency Shift due to Non-uniform and Uniform distribution of E.coli cells**

The Values shown in the Table 4.2 are plotted as shown in Figure 4.4. We can notice the gradual increase of the frequency shift away from the linear plot of uniform distribution. Finally as the increasing layer of mass reaches the uniform distribution condition the two plots meet meaning no further mass could be attached over the sensor platform.

**Table 4.3 Calculated and Simulated Maximum Resonant Frequency Shift results for Non-Uniform Distribution**

No of <i>E.coli</i> cells	$\eta$	$\Delta f_{sim}$ (KHz)	$\Delta f_{cat}$ (KHz)
0	0	0	0
2394	0.006060759	54.4	54.06707
4790	0.012126582	105.6	107.2729
9578	0.024248101	190	211.7054
14366	0.03636962	242.4	312.6322
19156	0.048496203	264.2	413.5923
23948	0.060627848	267	514.6023

The Non-uniform distribution of *E.coli* cells was carried out by Numerical simulation following the boundary conditions and applying the material properties as required to perform the modal analysis. The simulation results were obtained and corresponding theoretical values were also calculated using the Equation developed as shown in Table 4.3. These values were plotted against Number of *E.coli* cells that were assumed to be attached the sensor platform as shown Figure 4.5. From the Figure we notice that the theoretical values as tend to move away from the simulated plot as the number of cells increase. This could be explained by the fact that infinite point load at the free end would lead to very high frequency shift according to the vibration mechanism. Our equation is developed based on that factor but experimentally and in Numerical simulation we consider the practical possibility of the case which is nothing but the arrangement of cells as a layer with no two cells being attached one over the other. Hence we notice the deviation in the plot.

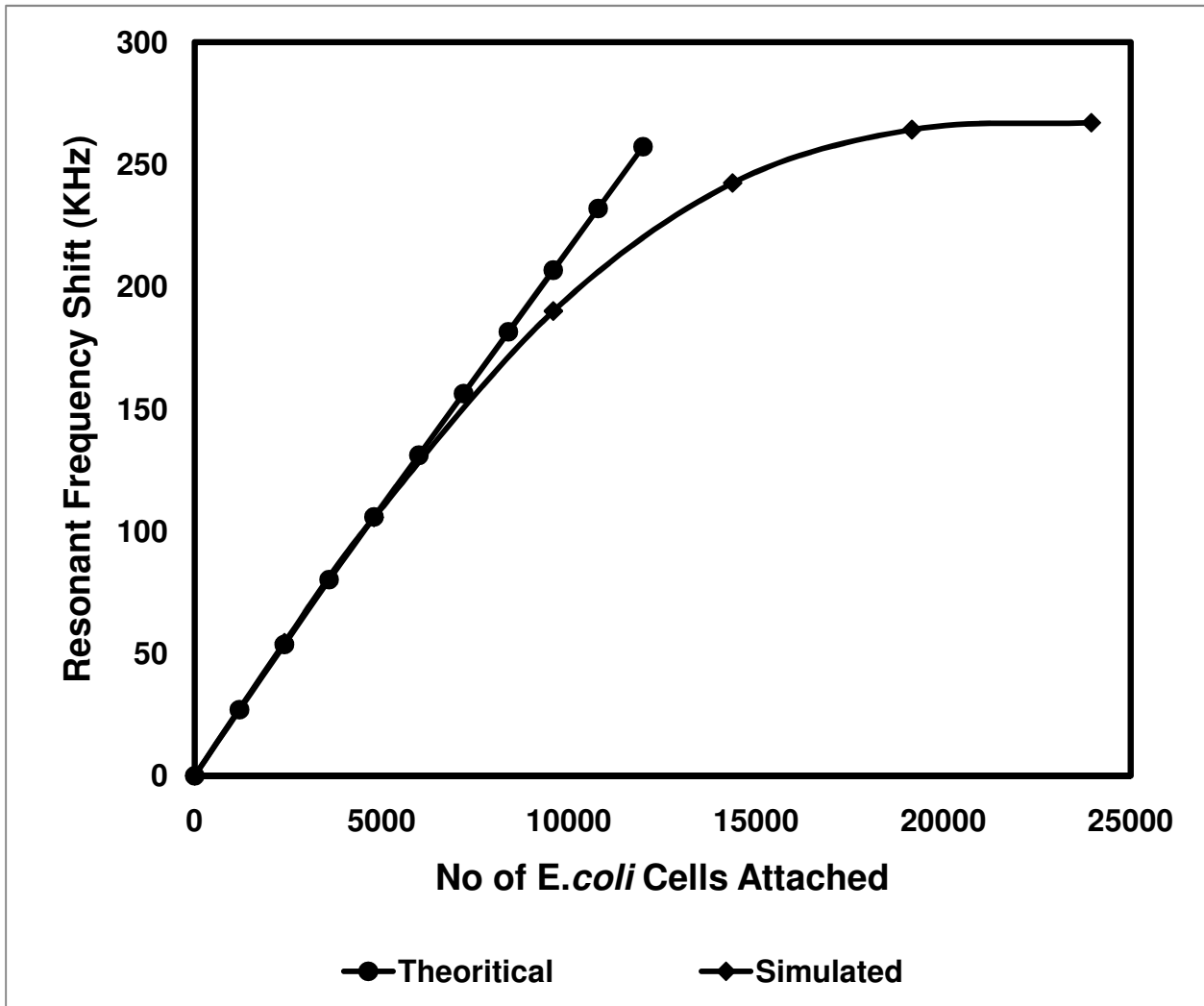


**Figure 4.6** Plots representing the Maximum Resonant Frequency Shift due to Non-uniform distribution of *E.coli* cells for Numerical Simulation and Theoretically calculated results.

### 4.1.2.2 Minimum Frequency Shift

The other important part of the Non-Uniform Distribution of Mass over the sensor platform is the Minimum Frequency shift case. This case is carried out through simulation by having the layers of *E.coli* cells distributed from the centre moving along the length till the layer completely covers the sensor platform to denote the uniform distribution case towards the end as shown in Figure 4.6.

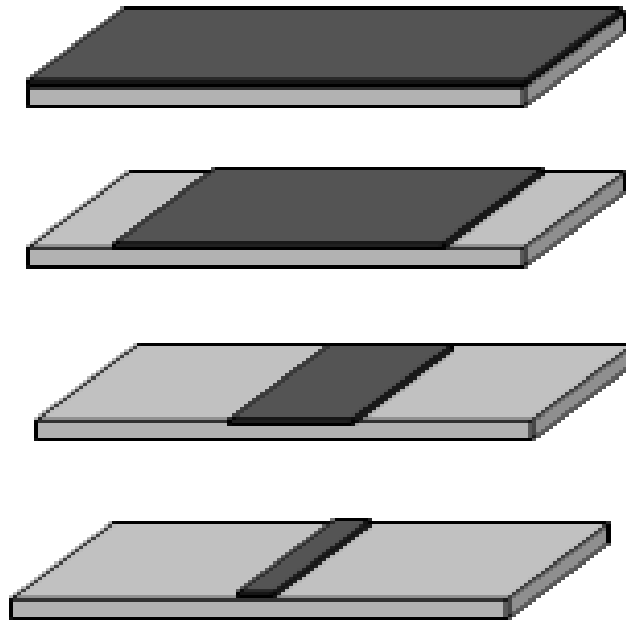


**Figure 4.7 Schematic diagrams representing the non-uniform distribution for the minimum resonant frequency condition**

Mathematically speaking the frequency shift for a certain amount of mass will have a tolerance limit based on their location and distribution. From the Equation (4.12) we know that the maximum frequency shift for certain amount of mass is observed at the free ends of the sensor



platform. This eventually explains the fact that the minimum frequency shift for the same amount of mass would be observed when concentrated at the centre. When mass is distributed close to the nodal point since the deformation experienced is relatively lower compared to the free ends , we observe minimum frequency shift close the centerline of the sensor platform. Considering these facts and using the equation of range

$$\Delta f_{uni} = \frac{\Delta f_{max} + \Delta f_{min}}{2} \quad (4.13)$$

Substituting (3.6) and (4.12) in (4.13)

We get 
$$\Delta f = -f_o \left\{ \eta + \left( \frac{KL}{2\pi} \right) - 1 \right\} \quad (4.14)$$

We were able to formulate an equation for minimum frequency shift due to concentration of mass at the centre of the sensor platform.

**Table 4.4 Calculated values of  $\eta$  and KL with the corresponding resonant frequency shift values determined using the Equation (4.14) and (3.6)**

$\eta$	0	0.0005	0.005	0.01	0.05	0.5	1	$\infty$
KL	$\pi$	3.1400225	3.125965	3.110498	2.99304	2.28893	2.02876	$\pi/2$
$\Delta f_{min}$ (KHz)	0	0.0018	0.226	0.909	24.185	2036.224	5731.441	$\infty$
$\Delta f_{uni}$ (KHz)	0	2.226	22.269	44.539	222.695	2218.825	4437.650	$\infty$

Table 4.4 shows the calculated values of  $\eta$  and KL with the corresponding resonant frequency shift values determined using the Equation (4.14) for the Minimum Frequency shift condition and Uniform distribution of *E.coli* cells using the Equation (3.6). From the values we notice that

$\Delta f_{min}$  decreases gradually with the increase in the number of cells attached to the sensor platform compared to the  $\Delta f_{uni}$  values noticed in the table. The Minimum Resonant Frequency shift values were plotted against the number of cells attached as shown in Figure 4.7. The plots show that initially there was zero frequency shift in both the cases since no mass was attached to the sensor platform. And also the final values for the both the cases seems to meet at the same point meaning that the cells are distributed throughout the sensor platform as the number increases.

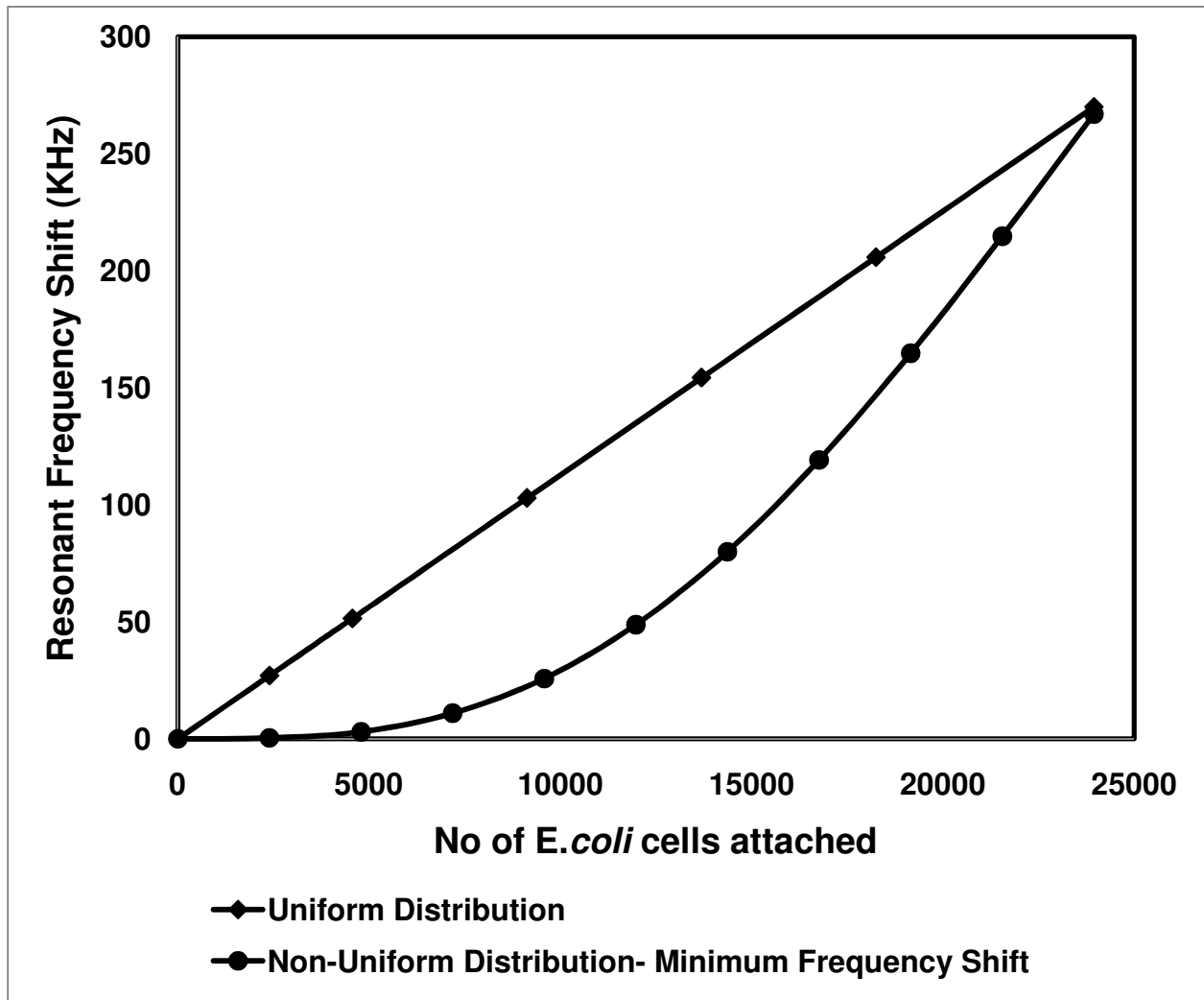
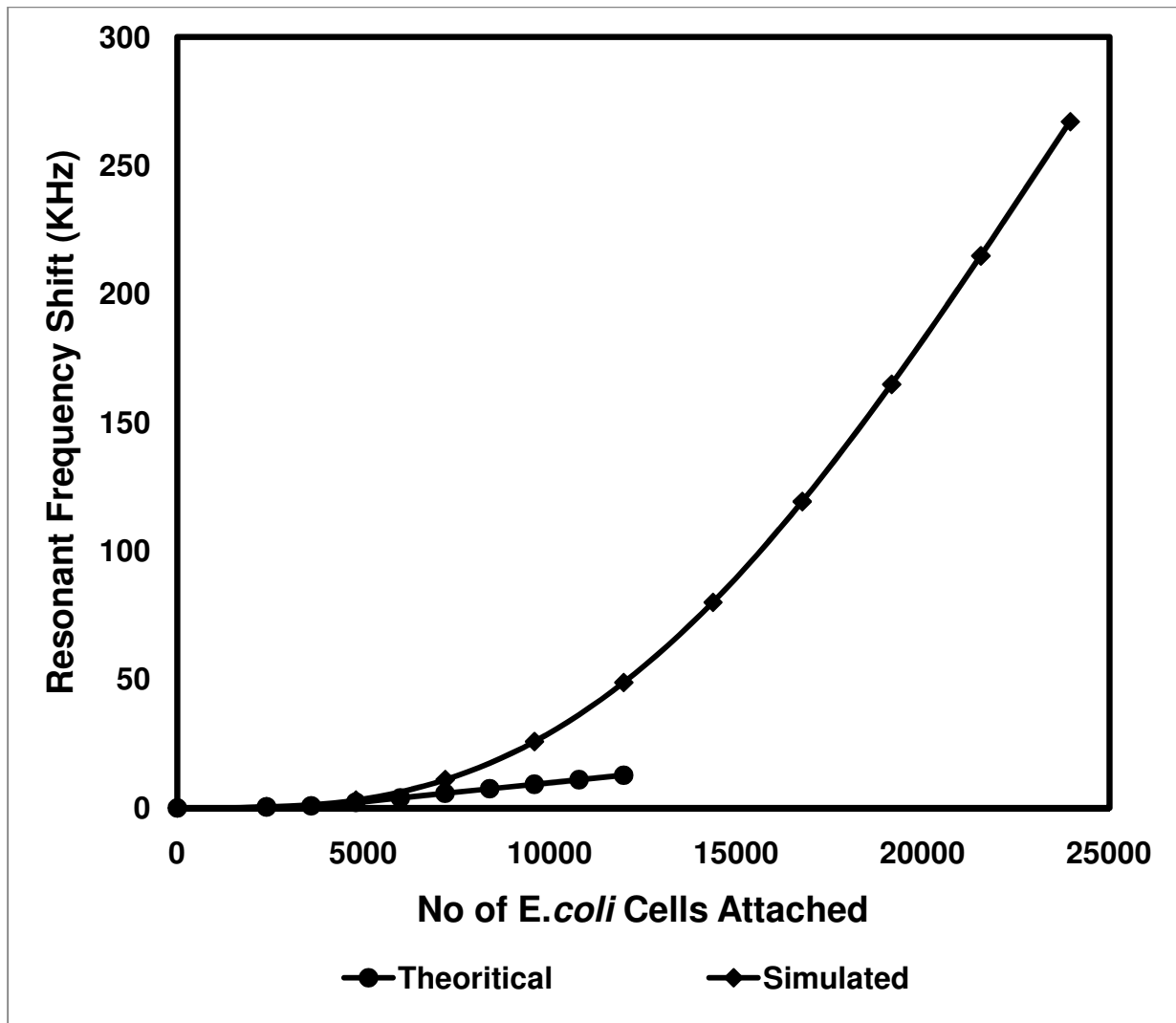


Figure 4.8 Plots representing the Minimum Resonant Frequency Shift due to Non-uniform and Uniform distribution of E.coli cells

**Table 4.5 Calculated and Simulated Minimum Resonant Frequency Shift results for Non-Uniform Distribution**

No of <i>E.coli</i> cells	$\eta$	$\Delta f_{sim}$ (KHz)	$\Delta f_{cal}$ (KHz)
0	0	0	0
2394	0.006061	0.4	0.079
4790	0.012127	3	0.748292
9578	0.018187	25.8	4.291807
14366	0.024248	80	11.3411
19156	0.030309	164.8	18.40219
23948	0.03637	267	25.45843

Table 4.5 presents the calculated and simulated minimum resonant frequency shift results for non-uniform distribution. The values clearly depict the fact that simulated values are much higher compared to the calculated values. This could be due various factors and one among them is fact that infinite point load at the nodal point does not constitute to any frequency shift. From the Figure 4.8 we can also notice that after a certain amount of the mass the movement of the theoretical plot deviate in a linear manner compared to the simulation plot which is mainly due to the assumption made in accordance to the distribution of load along the free ends. but in reality as the mass increases it moves closer to the nodal point and eventually meet the uniform distribution line at a particular amount of mass which is the same in case of minimum frequency shift of the sensor due to mass distribution.



**Figure 4.9 Plots representing the Minimum Resonant Frequency Shift due to Non-uniform distribution of *E.coli* cells for Numerical Simulation and Theoretically calculated results.**

In the previous two sections we discussed the major factor that affects the Resonant Frequency of the sensor which was focused in detail for the detection of biological specimens. The Equations were formulated to verify the results obtained by numerical simulations. Figure 4.9 provides the complete tolerance limit of the possible frequency shift that could be expected from the sensor when subjected to longitudinal vibration mode due to the distribution of mass. The

sensor dimension considered for the above cases was  $250\mu\text{m} \times 50\mu\text{m} \times 4\mu\text{m}$  with *E.coli* of size  $1.43\mu\text{m} \times 0.73\mu\text{m} \times 0.73\mu\text{m}$ .

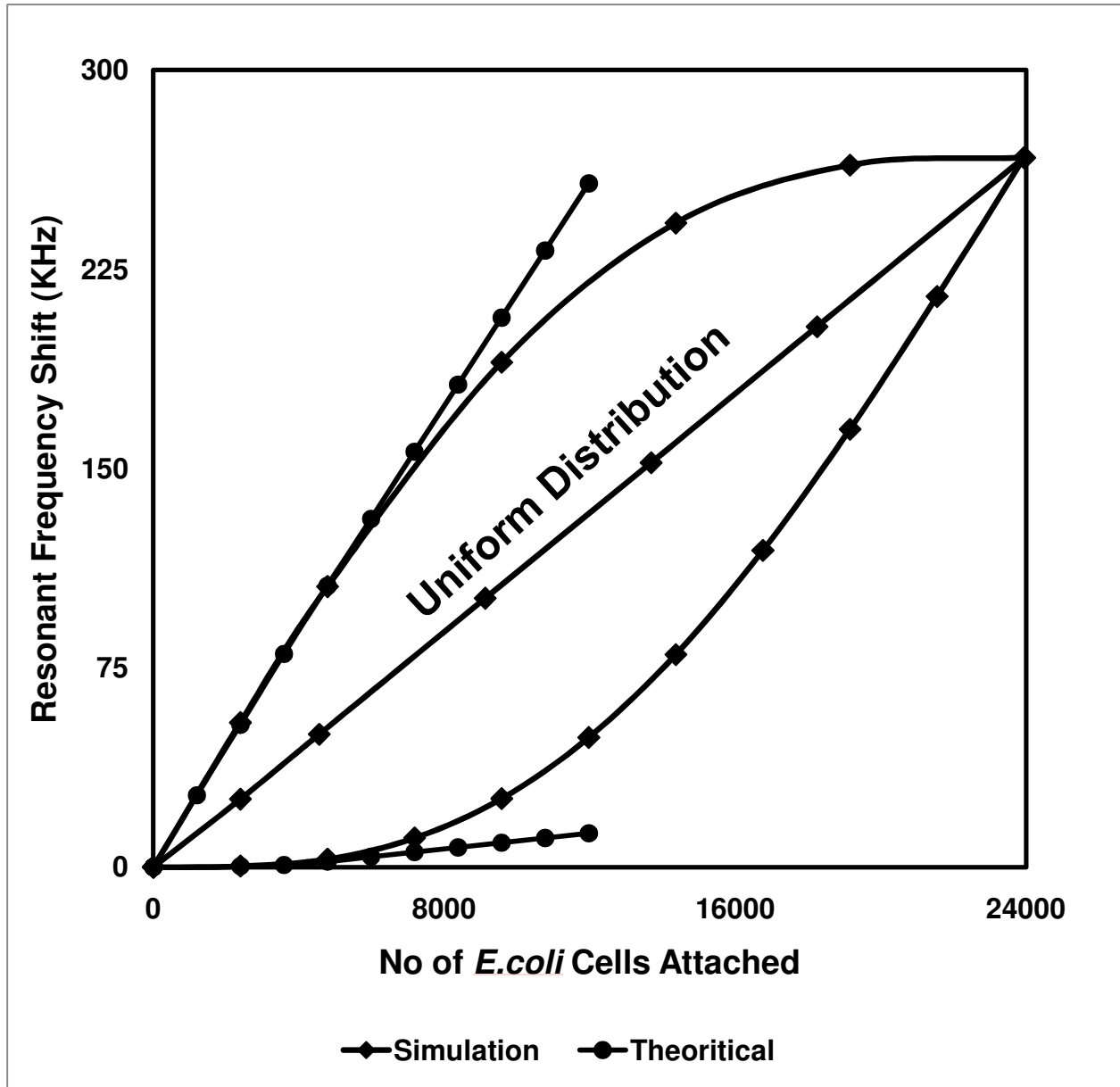
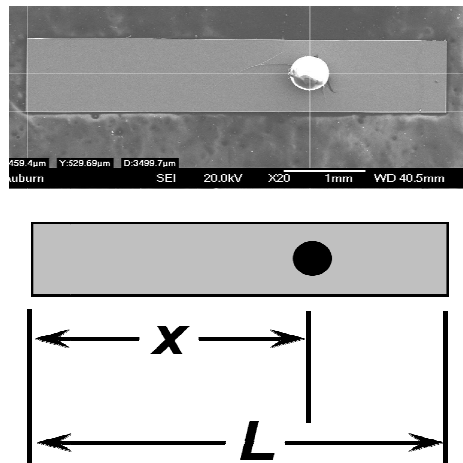


Figure 4.10 Plots representing the Resonant Frequency Shift of the sensor platform of dimension  $250\mu\text{m} \times 50\mu\text{m} \times 4\mu\text{m}$  due to distribution of mass(*E.coli* cells of size  $1.43\mu\text{m} \times 0.73\mu\text{m} \times 0.73\mu\text{m}$ .)

## 4.2 Influence of Discrete Position

### 4.2.1 Simulation Results

Tolerance limit of frequency shift depends on the position of the mass attached irrespective of the amount of mass involved. When mass becomes attached to the sensor platform, it effectively dampens the speed of the deformation waves propagating in the strip, which reduces its resonant frequency. In this case, where the attached mass is a discrete mass bonded in a particular location as shown in Figure 4.10, the wave speed on the side of the attached mass is less than the opposite side where no mass is attached.









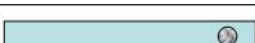


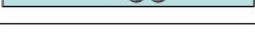

or platform of

Numerical simulation was carried out by attaching a layer of dimension  $25\mu\text{m} \times 50\mu\text{m} \times 0.73\mu\text{m}$  which accounts to 1200 *E.coli* cells considering the density and size of a single cell. This particular layer was attached at discrete locations and the frequency shift was noted. The reason for the usage of a thin layer in place of discrete mass is due to the decimal value result obtained using the sensor and the sensitivity level of the software tool in recognizing the discrete mass addition in providing the corresponding frequency shift.

## 4.2.2 Experimental Results

Beads were also positioned away from the longitudinal center axis of the sensor to assess the influence of lateral position for the same longitudinal position  $x$ . Test number 7 in Table 4.6 illustrates this positioning in reference to Test number 1. The frequency shift was relatively unaffected indicating that lateral positioning for a discrete mass addition was negligible in comparison to longitudinal positioning. Table 4.6 lists the results from the first harmonic mode resonance behavior of the sensors before ( $f_0$ ) and after ( $f$ ) bead attachment. Note that  $x$  denotes the relative position for a single bead attached on the sensor. As the bead was successively positioned further from the center of the strip, it had increased influence on the resonant frequency, increasing from 66 Hz at test position 1 to 30,900 Hz at test position 6.

**Table 4.6 Test results of sensor (5 mm x 1 mm x 28  $\mu$ m) attached with glass bead at different locations[29]**

test	$f_0$ (kHz)	$f$ (kHz)	$\Delta f$ (kHz)	$\frac{\Delta f}{f_0}$	X (mm)	Glass bead location 
1	443.334	443.268	-0.066	-0.00015	X=2.518	
2	438.400	438.468	0.068	+0.00016	X=2.482	
3	438.268	435.668	-2.600	-0.0059	X=3.010	
4	442.134	435.000	-7.134	-0.0161	X=3.460	
5	438.934	422.834	-16.100	-0.0367	X=3.682	
6	438.100	412.634	-25.466	-0.0581	X=4.392	
7	439.468	408.568	30.900	0.0682	X=4.942	
8	441.334	438.234	-3.100	0.0070	X1=2.668 X2=2.182	
9	437.668	411.634	-26.034	-0.0595	X1=4.818 X2=2.475	
10	441.200	397.900	-43.300	-0.0981	X1=4.908 X2=0.248	

The values from Table 4.6 are calibrated according to the Numerical simulation and theoretical calculation dimensions of the sensor and *E.coli* cells. The discrete mass value was normalized for the sensor dimension 250 $\mu\text{m}$  x 50 $\mu\text{m}$  x 4 $\mu\text{m}$  considering the size of *E.coli* cell to polystyrene glass beads that was used for experimental results.

### 4.2.3 Theoretical Verification

During resonance, the wave frequency must match on either side of the sensor. In order to account for the imbalance of wave speeds, the zero nodal point must shift such that the distance the waves travel on each side enables the waves to arrive at the nodal point at the same time to ensure they are in phase. Considering the mode shape factor for a free standing beam which is given as  $\cos\left(\frac{i\pi x}{L}\right)$  where  $i=1,2,3,\dots$ . And combining it with the results obtained by experimental method and finite element simulation we were able to develop the Equation 4.11 as shown below:

$$\Delta f = \frac{-f_o}{2} \left( \frac{\Delta m}{m_{sen}} \right) \left\{ 1 - \cos\left(\frac{\pi x}{L}\right) \right\} \quad (4.15)$$

This Equation would provide us with the resonant frequency shift of the sensor platform due to a concentrated mass at discrete positions over the sensor. Thus as the attached mass was moved further from the node its influence increased dramatically, see Figure 4.11. In this case it must shift towards the side with the attached mass. Thus, as the mass is moved further away from the original nodal point, the wave speeds are increasingly imbalanced and the node must shift further to account for it, resulting in larger frequency shifts. The trend for the freestanding beam



followed the experiments with larger responses as the mass was positioned towards the free end. Both curves resemble a full cycle cosine function of the form, which is similar to the longitudinal mode shape and amplitude of displacement defined elsewhere[35].

**Table 4.7 The Resonant Frequency shift values corresponding to concentrated mass on discrete locations**

Theoretically Calculated		Experimental Result		Numerical Simulation	
(X/L)	$\Delta f$ (KHz)	(X/L)	$\Delta f$ (KHz)	(X/L)	$\Delta f$ (KHz)
0	26.89583241	0.0116	30.9	0.05	26.5
0.1	24.32750895	0.1216	25.466	0.15	21.5
0.2	17.60355085	0.2636	16.1	0.25	13.6
0.3	9.292281557	0.308	7.134	0.35	5.7
0.4	2.568323456	0.398	2.6	0.45	0.8
0.5	0	0.4964	0.066	0.5	0.1
0.6	2.568323456	0.602	2.6	0.55	0.8
0.7	9.292281557	0.692	7.134	0.65	5.7
0.8	17.60355085	0.7364	16.1	0.75	13.6
0.9	24.32750895	0.8784	25.466	0.85	21.5
1	26.89583241	0.9884	30.9	0.95	26.5

The values shown in Table 4.7 clearly depict the fact that the resonant frequency shift obtained in the sensor due to concentration of mass at discrete locations form a cosine wave plot. This describes the mass distribution concept also showing that the frequency shift is higher at the free ends and gradually decreases as the mass moves towards the central nodal point. The values obtained by experimental and numerical simulation method abides by the theoretically calculated values.

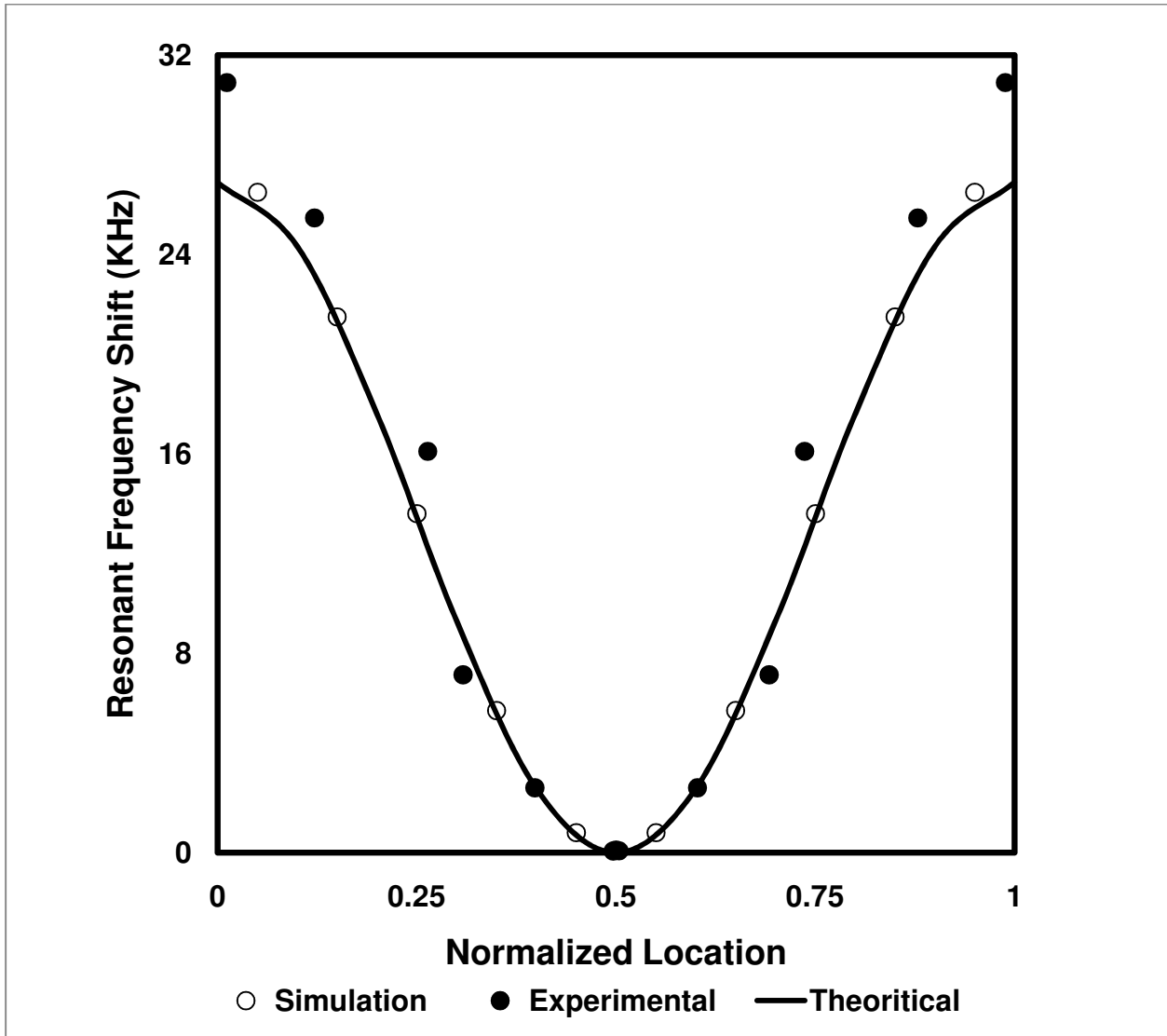


Figure 4.12 Plots of Resonant Frequency shift in KHz for the addition of concentrated mass at discrete locations over the sensor platform

## **4.3 Influence of Physical Dimension**

The previous sections involved the mass distribution and discrete location of concentrated mass as factors affecting the resonance behavior of the sensor platform. Another important factor that affects the resonance behavior of the system is the physical dimension of the sensor. This section describes the influence of length and width of the sensor platform in resonance behavior. The thickness is not separately explained since it would have the same effect as width over the sensor's behavior for the longitudinal vibration mode which would be explained in detail in the width dependence section. Both the cases the mass attachment was very similar to the one we discussed in the previous sections except for the increase in length or width of the sensor.

### **4.3.1 Length Dependence**

Simulations were carried out to study the effect of variation in resonance behavior due to change in dimensions of the sensor. Figure 4.12 show that variation in length of the sensor has a dramatic effect on the frequency shift. When the sensor is subjected to Longitudinal vibration, due to the sensor materials magnetic property the deformation occurs in the longitudinal direction along the direction of the applied field. The larger the length of the sensor greater is the sensitivity and hence greater resonant frequency shift for the same amount of mass.

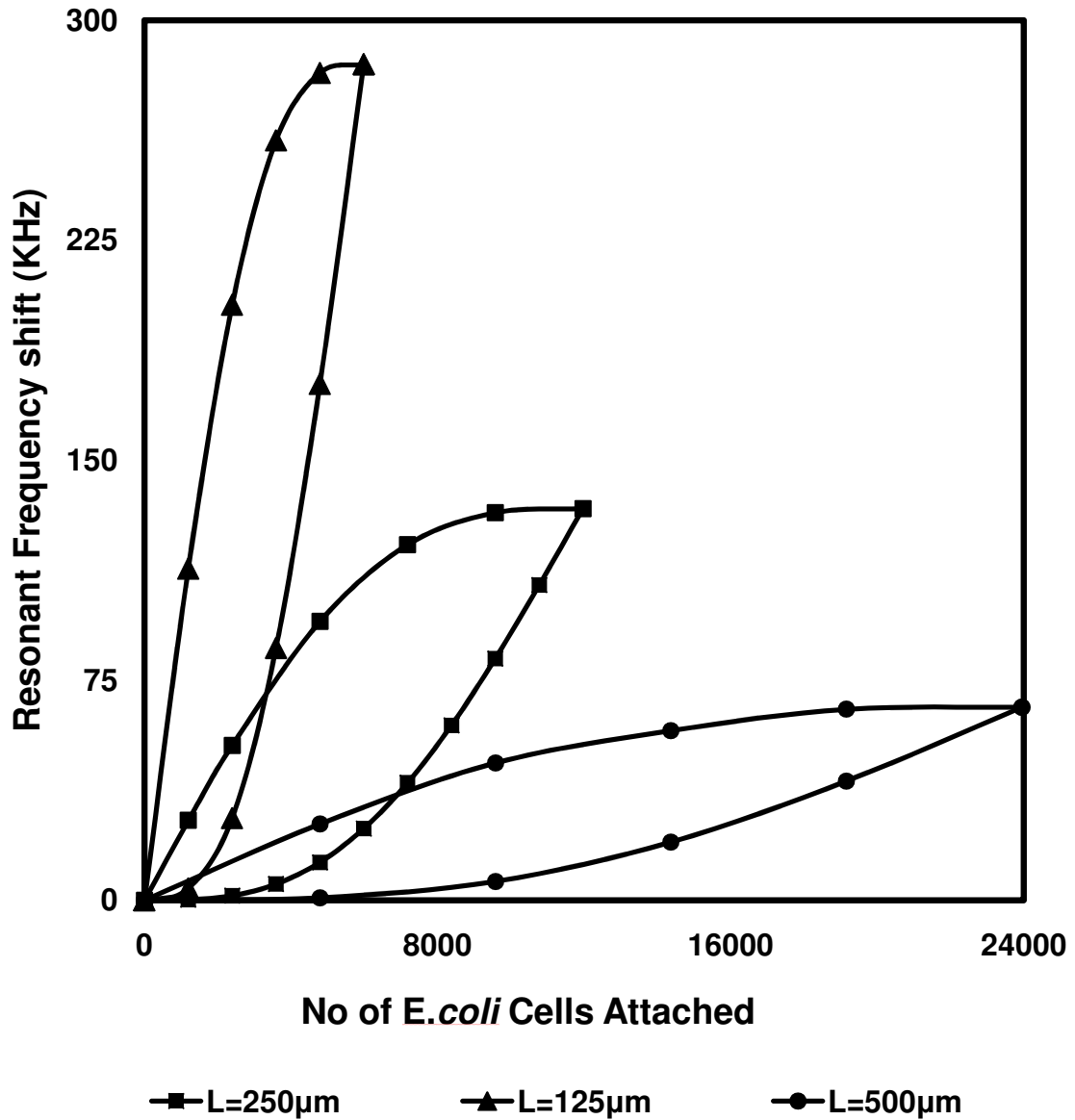


Figure 4.13 Plots of Resonant Frequency shift due to mass distribution over the sensor platform with varying Length

### 4.3.2 Width Dependence

In Figure 4.13 variation in width of the sensor platform does not have any influence on the acoustic response of the sensor. This is because lateral axis of the sensor does not experience any deformation due to their restricted boundary conditions and hence distribution of mass is considered to uniform along the lateral distance at any point on the sensor platform. This is experimentally proved with the help of polystyrene glass beads that had no influence on the resonant frequency shift when attached along their lateral position of the sensor platform.

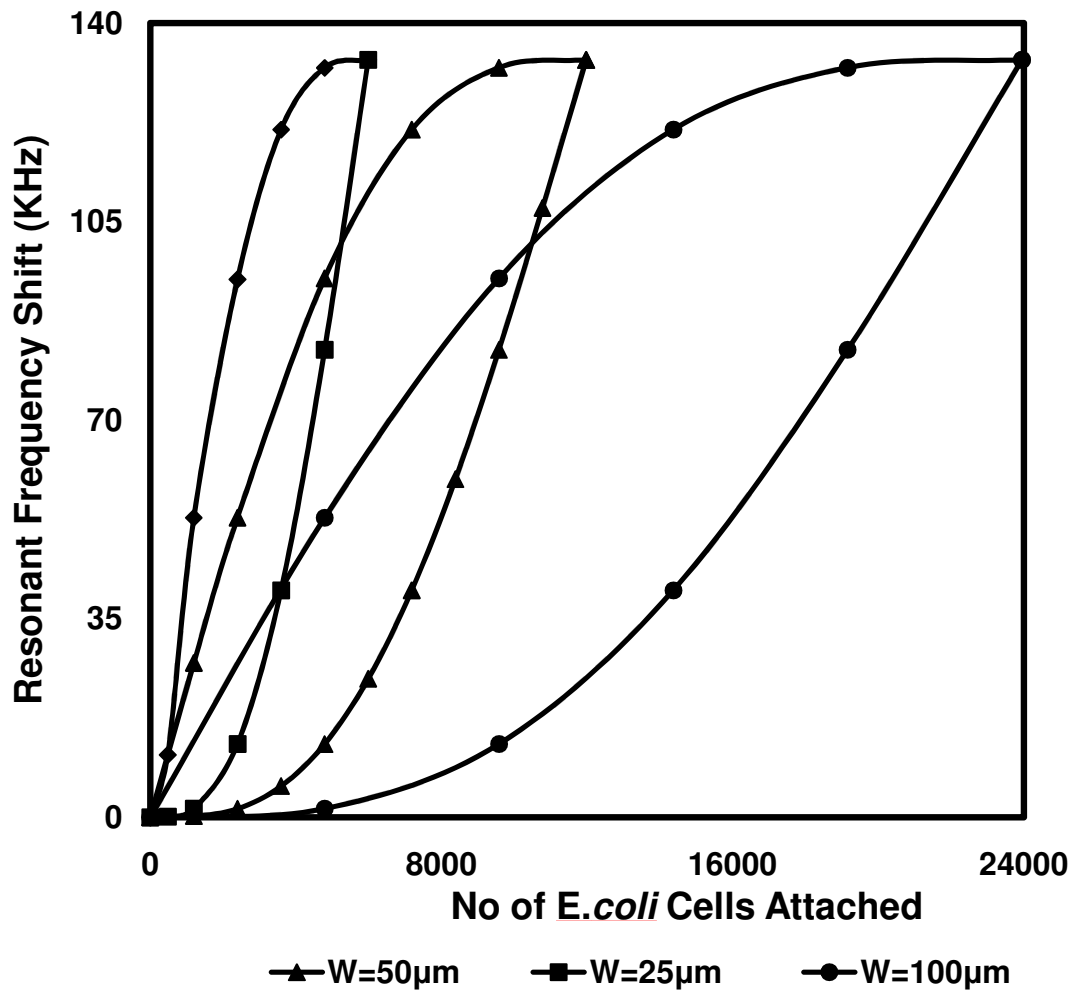


Figure 4.14 Plots of Resonant Frequency shift due to mass distribution over the sensor platform with varying Width

## **CHAPTER 5**

### **CONCLUSION**

A Model developed based on the acoustic response of Magnetostrictive Sensor actuated longitudinally with the modulated magnetic field. Numerical simulations and experimental verifications were carried out with the predicted model considering the factors influencing the resonance behavior of the sensor. The tolerance limit of frequency shift corresponding to the distribution of mass, discrete position of the mass attached and the physical dimensions of the sensor platform were determined in several ways. A Good agreement was found between these results offering a good paradigm for detecting biological agents.

## REFERENCES

1. Velusamy, V., et al., *An overview of foodborne pathogen detection: In the perspective of biosensors*. Biotechnology Advances. **28**(2): p. 232-254.
2. Mello, L.D. and L.T. Kubota, *Review of the use of biosensors as analytical tools in the food and drink industries*. Food Chemistry, 2002. **77**(2): p. 237-256.
3. Lazcka, O., F.J.D. Campo, and F.X. Muñoz, *Pathogen detection: A perspective of traditional methods and biosensors*. Biosensors and Bioelectronics, 2007. **22**(7): p. 1205-1217.
4. Griffin, G.D., D.N. Stratis-Cullum, and S. Moselio, *Biosensors*, in *Encyclopedia of Microbiology*. 2009, Academic Press: Oxford. p. 88-103.
5. Huang, S., et al., *Sequential detection of Salmonella typhimurium and Bacillus anthracis spores using magnetoelastic biosensors*. Biosensors & Bioelectronics, 2009. **24**(6): p. 1730-1736.
6. Ivnitski, D., et al., *Biosensors for detection of pathogenic bacteria*. Biosensors and Bioelectronics, 1999. **14**(7): p. 599-624.
7. Bhunia, A.K. and L.T. Steve, *Biosensors and Bio[hyphen (true graphic)]Based Methods for the Separation and Detection of Foodborne Pathogens*, in *Advances in Food and Nutrition Research*. 2008, Academic Press. p. 1-44.
8. Nayak, M., et al., *Detection of microorganisms using biosensors--A smarter way towards detection techniques*. Biosensors and Bioelectronics, 2009. **25**(4): p. 661-667.
9. Grate, J.W., S.J. Martin, and R.M. White, *Acoustic-Wave Microsensors .1*. Anal. Chem., 1993. **65**(21): p. A940.

10. Ballantine, D.S., et al., *Acoustic Wave Sensors: Theory, Design, and Physical-chemical applications*. 1997, New York: Academic Press.
11. Thundat, T., P.I. Oden, and R.J. Warmack, *Microcantilever sensors*. *Microscale Thermophys. Engr.*, 1997. **1**(3): p. 185.
12. Ilic, B., et al., *Single cell detection with micromechanical oscillators*. *J. Vac. Sci. Tech. B*, 2001. **19**(6): p. 2825.
13. S.Q., L., et al., *Biosensor Based on Magnetostrictive Microcantilevers as a Sensor Platform*. *Appl. Phys. Lett.*, 2006. **88**: p. 073507.
14. Li, P., et al., *A magnetoelectric energy harvester and management circuit for wireless sensor network*. *Sensors and Actuators a-Physical*. **157**(1): p. 100-106.
15. <http://www.metglas.com/>.
16. Schmidt, S. and C.A. Grimes, *Characterization of nano-dimensional thin-film elastic moduli using magnetoelastic sensors*. *Sens. Act. A*, 2001. **94**(3): p. 189.
17. Wan, J., et al., *Phage-Based Magnetoelastic Wireless Biosensors for Detecting Bacillus Anthracis Spores*. *IEEE Sens. J.*, 2007. **7**(3): p. 470-477.
18. Dover, J.E., et al., *Recent advances in peptide probe-based biosensors for detection of infectious agents*. *Journal of Microbiological Methods*, 2009. **78**(1): p. 10-19.
19. Ward, M.D. and D.A. Buttry, *In situ Interfacial Mass Detection with Piezoelectric Transducers*. *Science*, 1990. **249**(4972): p. 1000.
20. Suwa, Y., et al., *Study of Strain Sensor Using FeSiB Magnetostrictive Thin Film*. *Ieee Transactions on Magnetics*. **46**(2): p. 666-669.
21. Raiteri, R., et al., *Micromechanical cantilever-based biosensors*. *Sens. Act. B*, 2001. **79**(2-3): p. 115.



22. Bian, L.X., Y.M. Wen, and P. Li, *The field dependence of magnetoelastic damping in magnetostrictive material and its application in the magnetic field sensing*. Acta Physica Sinica. **59**(2): p. 883-892.
23. Morshed, S., et al., *Modifying Geometry to Enhance the Performance of Microcantilever-Based Acoustic Sensors*. Sensor Letters, 2009. **7**(1): p. 38-41.
24. Morshed, S. and B.C. Prorok, *Tailoring beam mechanics towards enhancing detection of hazardous biological species*. Experimental Mechanics, 2007. **47**(3): p. 405-415.
25. Liang, C., S. Morshed, and B.C. Prorok, *Correction for longitudinal mode vibration in thin slender beams*. Applied Physics Letters, 2007. **90**(22).
26. Liang, C. and B.C. Prorok, *Measuring the thin film elastic modulus with a magnetostrictive sensor*. Journal of Micromechanics and Microengineering, 2007. **17**(4): p. 709-716.
27. Park, C.S., et al., *Dimensionally gradient magnetoelectric bimorph structure exhibiting wide frequency and magnetic dc bias operating range*. Journal of Applied Physics, 2009. **106**(11).
28. Ong, K.G., et al., *A rapid highly-sensitive endotoxin detection system*. Biosens. Bioelec., 2006. **21**(12): p. 2270.
29. Cai, L., *"Development of Bulk-scale and Thin film Magnetostrictive Sensor"*, in *Materials Engineering*. 2007, Auburn University Auburn. p. 1-258.
30. Mungle, C., C.A. Grimes, and W.R. Dreschel, *Magnetic field tuning of the frequency-temperature response of a magnetoelastic sensor*. Sens. Act. A, 2002. **101**(1-2): p. 143.

31. Stoyanov, P.G., et al., *A remotely interrogatable sensor for chemical monitoring*. IEEE Trans. Mag., 1998. **34**(4): p. 1315.
32. Guntupalli, R., et al., *A Magnetoelastic Resonance Biosensor Immobilized with Polyclonal Antibody for the Detection of Salmonella Typhimurium*. Biosens. Bioelec., 2007. **22**(7): p. 1474-1479.
33. Huang, S., et al., *The effect of annealing and gold deposition on the performance of magnetoelastic biosensors*. Materials Science & Engineering C-Biomimetic and Supramolecular Systems, 2008. **28**(3): p. 380-386.
34. Johnson, M.L., et al., *A wireless biosensor using microfabricated phage-interfaced magnetoelastic particles*. Sens. Act. A, 2008. **144**: p. 38.
35. Blevins, R.D., *Formulas for natural frequency and mode shape*. 2001, Malabar, FL. USA: Krieger Publishing Company. pp. 183-184.